Norwegian University of Life Sciences

Master's Thesis 2021 60 ECTS

Faculty of Environmental Sciences and Natural Resource Management

Exposure assessment and particle characterization of workplace aerosols in Norwegian metal laser-cutting industry

Johanne Østereng Halvorsen

Master in Chemistry

Preface

This thesis marks the end of a two-year run for a master's in chemistry at the Faculty of Environmental Sciences and Natural Resource Management (MINA), at the University of Life Sciences (NMBU). It continues a pilot study on particulate pollution in laser-cutting industry conducted by The National Institute of Occupational Health in Norway (STAMI).

First and foremost, I would like to thank my two supervisors Elin Lovise Folven Gjengedal (Associate Professor at NMBU) and Stine Eriksen Hammer (Scientist at STAMI). Thank you, Elin, for giving me academical challenges and opportunities. I cannot begin to describe how grateful I am for your support and the amount of work you put into all your students. Thank you, Stine, I appreciate all our discussions and your input has been of great value though both practical and theoretical work.

Thanks to STAMI and the Occupational Environmental Chemistry group for letting me join the project and letting me use both the SEM and ICP-MS. A special thanks to Torunn K. Ervik for teaching me EBSD analysis and all other help with the SEM. Lastly thank you STAMI for financing the thesis work.

The last six years at NMBU has been an adventure, thanks to all my friends and extended family in Ås. I would like to thank "Rappkjefta ryper" for your support, humour, and ability to brighten up even a never-ending pandemic. Furthermore, I would like to thank X-Mølla for your company and showing that coincidences may lead to the best of friends.

Lastly, thanks go to my family and partner for all their support throughout two bachelor's and a master's degree over the last six years. Thank you, mom, dad, and Arne-Magnus, for always believing in me. Thank you Torbjørn for calming words and good hugs, especially these last months.

To quote a cinematic masterpiece of which name should not be mentioned:

Now what?

Johanne Østereng Halvorsen

Abstract

Laser-cutting is a technique often used in metal processing where the energy of a laser beam is utilized to cut steel and other alloys. A fine aerosol called fume, is produced through vaporization and condensation of the cut material. Metal fume can cause adverse health effects, like metal fume fever, to workers exposed. A pilot study of exposure in the Norwegian laser cutting industry was made in 2019, but the overall exposure has not been assessed further.

An initial exposure assessment was made to follow up the pilot study and determine the workplace exposure to particulate matter (PM), along with the chemical and physical properties of particles from laser cutting. Particles were collected from three different sites utilizing a combination of open and enclosed laser cutters. The sites cut steel, aluminium, and titanium plates with thicknesses from 0.5 to 15 mm. Respirable dust was collected in accordance with NS-EN 689:2018 + AC:2019, through personal sampling devices, and analysed by gravimetric analysis and inductively coupled plasma mass spectrometry (ICP-MS). Particles from cutting specific materials were analysed by scanning electron microscopy (SEM) and ICP-MS. Bulk chemistry was determined by ICP-MS, while SEM was used for single particle analysis for particle morphology, relative atomic abundance by electron dispersive x-ray (EDX), and mineral phases by electron diffraction backscatter (EBSD). Real-time spectrometers were used for particle size distribution inside and outside of the laser cutters.

Metal fume particles from laser cutting consisted of primary particles from 10 nm and up to 200 nm geometric diameter in chainlike agglomerates/aggregates. The main size distribution of particles was within the respirable fraction; 30 to 350 nm, and the concentration of particles increased with decreasing plate thickness. The particles' chemical composition was like the original metal plate and the mineral phases seemed to be oxides of the main alloying elements.

The initial exposure assessment of a similar exposure group (SEG) revealed mentionable maximum air concentrations of aluminium (Al), copper (Cu), iron (Fe), magnesium (Mg), manganese (Mn), lead (Pb), tin (Sn), titanium (Ti), and zinc (Zn). However, all concentrations were below the OEL's set by the Norwegian Labour Inspection Authority (ATIL). The material cut on the day of sampling reflected the measured air concentrations. A 1000 times difference in air concentration between median and maximum value was measured. A higher total mass of respirable particles was found at the site with open laser cutters in comparison to enclosed laser cutters. A further exposure assessment specified for those who work with open-laser cutter are recommended to ensure acceptable exposure.

Sammendrag

Laserskjæring er en teknikk som ofte tas i bruk i metal produksjon, hvor en høyenergi laser brukes til å skjære stål og andre legeringer. Metallet blir fordampet, og vil senere kondensere og produsere en fin aerosol. Metallrøyk er kjent for å kunne ha en negativ helseeffekt, som metallfeber, på arbeidere som blir eksponert. En pilotstudie av eksponeringen har blitt utført, men eksponeringen i norske laserskjærings bedrifter har ikke blitt fullstendig kartlagt.

En forenklet undersøkelse ble utført for å bestemme arbeidsplass eksponering for støv på arbeidsplassen, og bestemme de kjemiske og fysiske egenskapene til partikler fra laserskjæring på metall. Partikler ble samlet hos tre ulike bedrifter, med en kombinasjon av åpne og innebygde laserskjærere. Det ble skåret på stål, aluminium og titan plater, med en platetykkelse fra 0,5 til 15 mm. Respirabelt støv ble samplet gjennom personbårne målinger etter NS:EN 689:2018 + AC:2019 standard og analysert med i induktivt koblet plasma massespektromerti (ICP-MS). Partikler fra skjæring på spesifikke materialer ble samlet for analyse med sveipeelektronmikroskop (SEM) og ICP-MS. Bulk kjemi ble bestemt ved bruk av ICP-MS, imens SEM ble brukt til enkeltpartikkelanalyse for bestemmelse av partikkel morfologi, relativt atom innhold ved Energidispersiv røntgendektektor (EDX) og et forsøk på å bestemme mineral fase ved elektron-tilbakespredning diffraksjon (EBSD). Samtids sprektrometri ble brukt for å bestemme størrelsesfordeling av partikler innenfor og utenfor laserskjærere.

Metallrøyk partiklene fra laserskjæring besto av primærpartikler med en geometrisk diameter fra 10 nm og opp til 200 nm i kjedelignende agglomerater/aggregater. Størrelsesfordelingen var hovedsakelig i den respirable fraksjonen fra 30 til 350 nm, og partikkelkonsentrasjonen økte med minkende platetykkelse. Partiklenes kjemiske sammensetning var avhengig av opphavsmaterialet og besto hovedsakelig av oksider av hovedkomponentene i legeringen.

Den forenklede eksponerings undersøkelsen av en sammenlignbar eksponert gruppe (SEG) viste markante maksimum luftkonsentrasjoner av aluminium (Al), kobber (Cu), jern (Fe), magnesium (Mg), mangan (Mn), bly (Pb), tin (Sn), titan (Ti) og sink (Zn). Alle målinger var under grenseverdiene satt av Arbeidstilsynet (ATIL). Materialene som ble skåret på var reflekter i de målte luftkonsentrasjonene. En variasjon på opptil 1000 ganger forskjell mellom maksimum og median konsentrasjon ble målt. En høyere total masse av partikulært materiale ble målt hos bedriften med åpne laserskjæere i motsetning til bedriftene med lukkede laserskjærere. En oppfølgende eksponerings undersøkelse anbefales for bedrifter med åpen laserskjærere for å sikre at eksponeringen er under grenseverdier.

Abbreviations

APS - Aerodynamic particle sizer

ATIL – Norwegian labour inspection authority (Norwegian: Arbeidstilsynet)

CEN – European committee for standardization

CRM – Certified reference material

EBSD – Electron diffraction backscatter

EDX – Electron dispersive X-ray

d_{ae} – aerodynamic diameter

d_g – geometric diameter

d_{mob} – mobility diameter

ICP-MS – Inductively coupled plasma mass spectrometry

LOD – Limit of detection

LOQ – Limit of quantification

OEL - Occupational exposure limit

PM – Particulate Matter

rat % - relative atomic percentage

SEG – Similar exposure group

SEM – Scanning electron microscopy

SMPS - Scanning mobility particle sizer

STAMI - The National Institute of Occupational Health in Norway (Norwegian: Statens arbeidsmiljøinstitutt)

TEM - Transmission electron microscopy

XRD – X-ray diffraction

List of tables

List of figures

Table of contents

Chapter 1 Introduction

Laser cutting is a well-known technique in the metal industry and offers significant advantages such as high precision, flexibility, and speed at low costs (Caristan, 2004; Molchanova et al., 2015; Yilbas et al., 2017). It is a thermal process that involves a heat source, the laser, concentrated on a material surface. The heat causes the material to vaporize, melt, or burn away, and is removed with an assist-gas pressure flow (Caristan, 2004). The high power laser can be used for cutting, drilling, cleaning, and marking on various materials, but is commonly used for metals (Majumdar & Manna, 2013). The technique has been shown applicable on non-metallic such as plastic, wood, cloth, glass, and stone depending on the laser source used (Eltawahni et al., 2011; Mushtaq et al., 2020; Nayak & Padhye, 2016; Riveiro et al., 2016; Solinov et al., 2015).

Metal fume is a fine aerosol produced when vaporized metal condenses in the air (Antonini, 2003; Ullmann et al., 2002). The particles from metal fume can cause a health risk to those exposed (Yassi et al., 2001). Inhalation of metal-containing fumes and gases can lead to adverse health effects such as metal fume fever, decreased pulmonary function, occupational asthma, bronchitis, and other respiratory illnesses (Antonini, 2003). The potential penetration of particles in the respiratory system is dependent on particle size (Cherrie & Aitken, 1999). Studies have indicated that the toxic response to metal fumes is dependent on the elemental composition of the particulate matter (PM) (McCarrick et al., 2019; McNeilly et al., 2004).

The Norwegian Labour Inspection Authority (ATIL) consider the potential health risks associated with laser- and other thermic-cutting, to be equal to the one of welding and dependent on the processed material (Arbeidstilsynet, 2021b). A pilot study conducted by The National Institute of Occupational Health in Norway (STAMI) in 2019 showed that most of the particles created by laser cutting had an aerodynamic diameter (d_{ae}) < 75 nm and that the total respirable mass concentrations were below the Norwegian occupational exposure limits (Hammer, 2019). Further studies of the exposure in the Norwegian laser cutting industry have not, to the best knowledge of the author, been conducted.

To investigate the impact of laser cutting in the workplace atmosphere and exposure to workers, will the metal fume particles formed be examined to determine both the workplace exposure and particle properties. The thesis aims to answer the following questions:

- What is the workplace exposure to PM in terms of air concentrations in a laser cutting work environment and the exposure within the limits set by The Norwegian Labour Inspection Authority?
- What are the physical and chemical properties like the morphology, size distribution, bulk chemistry, and mineral phase of particles from laser cutting?

These questions will be answered using different analytical techniques. The elemental composition of personal respirable dust samples, particles from cutting of specific materials, and dust from the ventilation systems will be determined by inductively coupled plasma mass spectrometry (ICP-MS) for total chemistry. Two different real-time spectrometers particle will be used for size distribution and number concentrations based on d_{ae} and mobility diameter (d_{mob}). Single particle analysis by operator-controlled scanning electron microscope (op-SEM) will provide information on the chemical and morphological properties of particles. Chemical composition will be determined by electron dispersive X-ray (EDX) and mineral phase by electron diffraction backscatter (EBSD).

Chapter 2 Workplace exposure to particulate matter

There are adverse health effects associated with workplace exposure to particulate matter. A well-known acute respiratory illness is metal fume fever, a result of inhalation of fumes, usually containing zinc (Zn), copper (Cu), magnesium (Mg), cadmium (Cd), nickel (Ni), aluminium (Al), manganese (Mn), silver (Ag), and/or vanadium (V) (Antonini, 2003; Graeme & Pollack, 1998; Yassi et al., 2001). High short term (15 to 75 min) workplace air concentrations of chromium (Cr), iron (Fe), Mn, Ni, and Cu in PM in the workers' breathing zone compared to 8-hour time-weighted-average has been reported for hot work processes with different steel materials (Berlinger et al., 2019). Studies have shown that the soluble fraction, and primarily soluble Cr, account for the toxic responses to stainless steel welding fume (McCarrick et al., 2019; McNeilly et al., 2004; Shoeb et al., 2017). Exposure to both hexavalent Cr and Ni compounds has been shown to increase risk of lung cancer and are human carcinogens (Berlinger et al., 2009; Cena et al., 2014; Gibb et al., 2000; Park et al., 2004). Moreover, inhaled Mn is associated with damage to the lungs, liver, and the central nervous system (Antonini et al., 2006b; Berlinger et al., 2009; Taube, 2013).

The particle size distribution is an important factor in determining the hazard potential of fume particles, in addition to particle chemistry. The information on particle size distribution provides an indication of the particle penetration in the lungs (Yassi et al., 2001). The particles entering the human respiratory system are divided into three different fractions depending on the region the particles may penetrate (Brown et al., 2013; CEN, 1993; Cherrie & Aitken, 1999):

- Inhalable fraction – the fraction of total airborne particles which is inhaled through the nose and mouth, failing to penetrate beyond the larynx.
- Thoracic fraction – the mass fraction of inhaled particles penetrating beyond the larynx into the trachea-bronchial regions.
- Respirable fraction – the mass fraction of inhaled particles penetrating the unciliated airways.

Particles with an $d_{ae} < 3$ µm tends to deposit in the lower portion of the respiratory tract where the airways become gradually smaller (Carvalho et al., 2011). The particle size of 4 µm d_{ae} has 50% penetration for the respirable fraction, see Figure 2.1, and almost 100% penetration at 1 µm d_{ae}. Particles with a greater particle size tend to deposit in the head airways. Larger particles, >100 µm, causes irritation in the nose, mouth, and eyes, but will not enter the rest of the respiratory system (Brown et al., 2013).

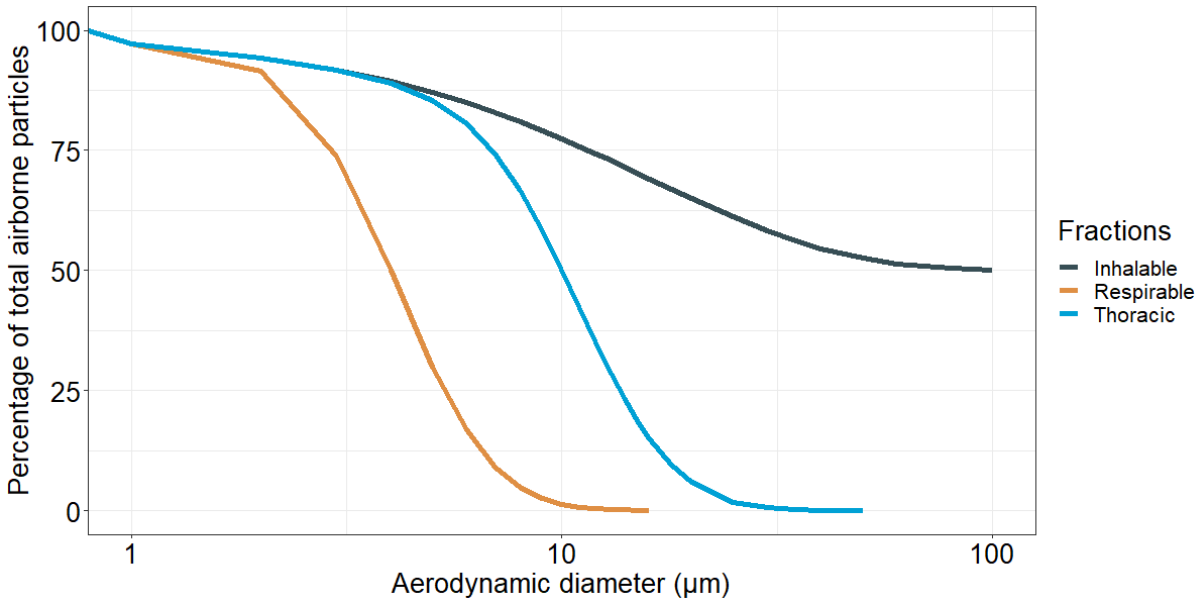

Figure 2.1 The inhalable, thoracic, and respirable fraction presented as the percentage of the total airborne particles. The figure is based on numerical values from EN 481:1993.

One of the goals of this thesis is to determine workplace exposure in the Norwegian laser cutting industry through general exposure measurements of the respirable dust. The particle size distribution will be determined to assess the penetration in the lungs in relation to exposure and health risk.

Chapter 3 Exposure assessment

The European Committee for standardization (CEN) approved a new standard (NS-EN 689:2018 + AC:2019) for measurement of workplace exposure by inhalation to chemical reagents in 2019 (CEN, 2019). The assessment of occupational exposure consists of a three-step strategy, see Figure 3.2. The exposure is found to be acceptable or not, after each step of the exposure assessment. If the exposure is to high measures must be taken. A written report must be made after an assessment. The exposure assessment is repeated every year or in the case of changes in the workplace.

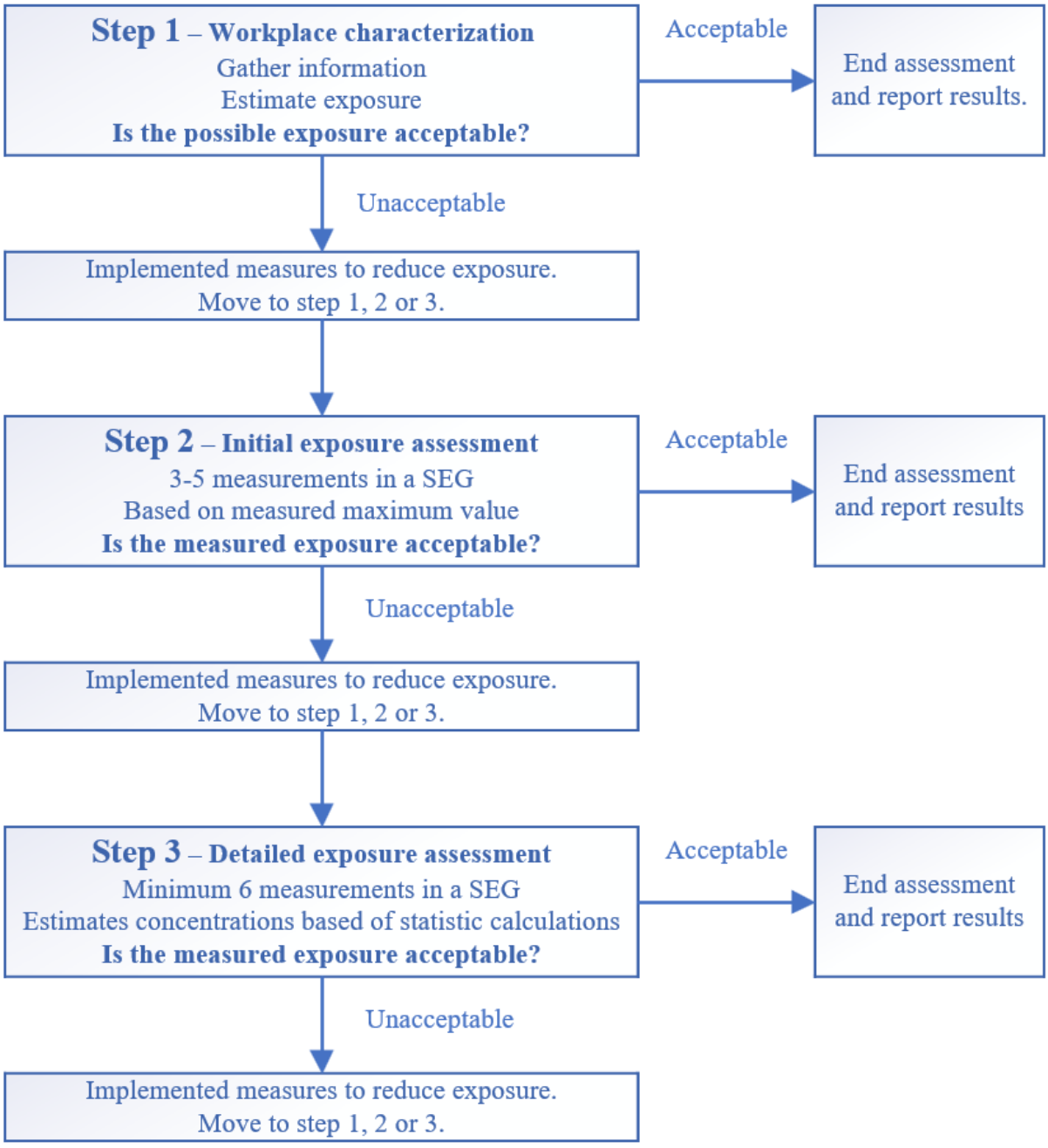

Figure 3.1 Flow Chart of the three different steps of exposure assessment

The first step in the exposure assessment is to get a general idea of the workplace exposure. An estimation of the exposure is made by gathering information on pollution sources relevant to OEL's, workplace factors and similar cases. The assessment is concluded if the risk of exposure is low and cause little to no health risk. An initial exposure measurement, step 2 in Figure 3.1, is initiated if the exposure is uncertain or believed to be higher than OEL's.

It is time-consuming to measure the exposure of each worker during each working day. Workers in a similar work environment, a similar exposure group (SEG), are selected to obtain a representative data set. It is expected that the exposure measured within the SEG is the case for all workers in the group, and a selection of random workers can be made for exposure sampling. Personal sampling devices should be used whenever possible when measuring possible exposure in a workplace environment (CEN, 2019). The sample device is placed within the breathing zone of the worker, 30 cm from the mouth and nose. The sampling duration must be representative of the task or for a working shift. The OEL's from ATIL presented, see Table 7.2, are based on 8-hour shifts. Short-term exposure has particular exposure limits that will not be used in this thesis.

Three to five samples representing the SEG should be collected in the second step of the exposure assessment. The highest measured value of each contaminant is then compared to the respective OELs. The maximum value of three samples must be ≤10% of the OEL's, ≤15% for four samples and ≤20% for five samples to be accepted.

The third step involves a detailed exposure assessment where at least six samples must be collected within the selected SEG. In this step, the results are tested statistically to determine if 95% of the exposure is below the OEL's with at least 70% confidence. The results are first determined to be either normal distributed or log-normal distributed. A log-normal distribution is most common as the measurements cannot be less than zero while there is in theory no upper limit (CEN, 2019). Equation 1 is used to find the upper confidence limit for comparison to OEL's with a log-normal distribution:

$$Upper\ confidence\ limit(0.95,0.70) = e^{(\bar{y}+U_T*SD_y)} \qquad \text{Equation 1}$$

x = measured air concentrations

y = ln(x)

$\bar{y}$ = The geometric mean of all y

U_T = statistical value dependent on number of samples found in the 2018 European standard

SD_y = Geometric standard deviation for y

Chapter 4 Laser cutting

Laser-cutting is a thermal process, utilizing the energy of a focused laser beam to melt or vaporize material in a localised area (Caristan, 2004). The word laser stands for light amplification by stimulated emission of radiation (Vanderwerf, 2017). The photons of the light beam are absorbed by the metal and the energy is converted into heat, causing the metal to melt and vaporize. The melted or vaporized metal is then removed from the cutting surface by a pressurized gas assistant jet. An inert or reactive gas is used, depending on material and type of laser. Nitrogen gas is often used when cutting stainless steel as it protects the surface from oxidation. Argon is another inert gas option, but is seldom used due to its higher cost. The use of a reactive gas, oxygen gas (O_2), or simply air, increases the temperature of the cutting area and cutting speed, which allows cutting of thicker material (Genna et al., 2020).

There are three main type of lasers used in laser cutting which all produce light within the infrared range (Vanderwerf, 2017):

- **CO_2-laser** uses low pressure carbon dioxide as the laser source and emits laser radiation at 10.6 µm wavelength. The laser beam is controlled using mirrors or lenses to cut or engrave materials.
- **Nd/YAG-laser** uses a cubic garnet crystal of $NdY_3Al_5O_{12}$ doped with neodymium ions as the laser medium. The laser can work at different energy levels which produce lasers in different wavelengths, from 266 to 1440 nm.
- **Fiber-laser** is an extension of Nd/YAG lasers and consist of thin silica glass fibre where the active medium is doped with a rare earth ion. The light is amplified through the fibre and the wavelength of the laser beam is dependent on the core material. Erbium emits laser with a wavelength between 1540 and 1560 nm, while yttrium emits wavelengths ranging from 980 to 1070 nm.

Most laser cutters have a computer numerical control system (CNC) to control the laser beam (Caristan, 2004). The workers oversee the process, as well as changing lenses, mirrors, and nozzles on the laser, maintenance and in some cases swapping out the plates manually.

Materials

Material selection is a question of choosing the material with the right characteristics for a specific application. The ability of a material to absorb energy and plastically deform without fracturing (toughness), to deform without fracturing (ductility), resistance to localized plastic deformation (hardness), and durability are some of the characteristics of the materials (Callister

& Rethwisch, 2020). These properties are dependent on the metal alloys, other additives, and manufacturing processes. Metal alloys can be grouped into two classes based on chemical composition, ferrous and nonferrous.

Ferrous alloys

Steel

Steels are a collective name for iron-carbon alloys which also contain other alloying elements, such as Cr, Mn, and Ni (Callister & Rethwisch, 2014). Steels are divided into low- and high-alloy steels and low- to high-carbon steel based on chemical composition. The mechanical properties are dependent on the carbon content, while alloying metals contribute to corrosion resistance, magnetic properties, strength, durability, and ductility. Plain carbon steel contains only residual impurities other than carbon and manganese, while alloy steels have alloying elements intentionally added in specific concentrations (Callister & Rethwisch, 2014).

Low-carbon steels: Contain less than 0.25 wt% carbon (C). These steels are relatively weak and soft, but have outstanding ductility and toughness. Low-carbon steels are unresponsive to heat treatment and strengthening of the steels are thereby done by cold work. Typical applications for low-carbon steels are automobile body components and structural shapes, while sheets of these steels may be used in the construction of buildings and bridges.

High-strength, low-alloy (HSLA) steels are a subgroup of low-carbon steels. These contain elements such as Cu, Ni, Mn, vanadium (V), and molybdenum (Mo) in concentrations up to 10 wt% which increase the strength and resistance to corrosion and preserve the ductility, formability, and machinability. The higher resistance to corrosion in comparison to plain carbon steel makes these steels useful in cases where both structural strength and corrosion resistance are important, as in pressure vessels and support columns in buildings.

Medium-carbon steels: Contain between 0.25 to 0.60 wt% C. Medium-carbon steels can undergo heat-treatment to improve mechanical properties. Plain medium-carbon steels can only be heat-treated in very thin sections and with a rapid quenching rate to improve strength (Callister & Rethwisch, 2014). The heat-treating capacity is increased by adding alloying metals like Cr, Ni, Mn, and Mo, giving various strength to ductility combinations and a wide range of applications. Applications include railway tracks, structural components, gears, and other machine parts.

High-carbon steels: The hardest, strongest, and least ductile of the carbon steels. These types contain between 0.60 to 1.4 wt% C. These steels are used in cutting tools and dies due to the high wear resistance. Alloying elements that give these properties are Cr, Mn, V, Tungsten (W), and Mo.

Stainless steel: Known for excellent resistance to corrosion due to a higher weight percentage of alloying elements, predominantly Cr (at least 11 wt%). Other main alloying elements are Ni, Mn, and Mo. Stainless steel is divided into three categories based on the predominant phase constituent of the microstructure: martensitic, ferritic, and austenitic. Austenitic stainless steel is the most corrosion resistant due to high concentrations of Cr, Mn, and Ni, and is equivalent to the Norwegian terminology "Syrefast stål".

Cast iron

Cast iron is a class of ferrous irons with a carbon content greater than 2.4 wt%. The carbon is, in most cast irons, in the form of graphite. The melting point of cast irons are considerably lower than steels, approximately 1150°C to 1300°C. Casting is the primary fabrication method of cast iron products due to its low melting point and the fact that some cast irons are very brittle.

Nonferrous alloys

Titanium and titanium-based alloys

Pure titanium (Ti) has a low density (4.5 g/cm^3), a high melting point (1668°C), and lower resistance to elastic deformation than steel (Callister & Rethwisch, 2014). Titanium alloys are strong and highly ductile. They are virtually immune to corrosion from air, marine, and industrial environments at normal temperatures. Titanium in combination with tin (Sn) has abilities to avoid permanent deformation under the influence of persistent mechanical stress. Common uses are in airplanes and in chemical and petroleum industries because of these mechanical properties and a relatively low density compared to steel (7.85-8.05 g/cm3). Alloying metals in titanium plates are aluminium (Al), Mo, V, Cu, and Fe (Callister & Rethwisch, 2020).

Aluminium and aluminium-based alloys

Aluminium, both pure and its alloys, have a relatively low density (2.7 g/cm^3), high electrical and thermal conductivities, and resistance against corrosion. Aluminium-alloys are easily manipulated due to their ductility, making it possible to produce thin sheets of aluminium. The chemical strength of aluminium can be enhanced by the addition of elements such as Cu, magnesium (Mg), silicon (Si), Mn, and zinc (Zn). Other less used alloying elements are Cr and lithium (Li).

Chapter 5 Metal fume

Metal fume is formed through nucleation as vaporized metal condenses in the air (Antonini, 2003). The results being a fine aerosol consisting of polydisperse solid particles in the fine (<2.5 µm) and ultrafine (<100 nm) size fractions (Keyter et al., 2019; Kulkarni et al., 2011). Primary particles from metal fumes are primarily spherical and can agglomerate or aggregate through collision, see Figure 5.1 (Antonini et al., 2006a; Sowards et al., 2010). Agglomerates are held together by weak physical interaction such as van der Waals forces or surface tension (Kulkarni et al., 2011). Aggregates, on the other hand, are formed when particles form a common crystalline structure resulting in a new larger particle (Eggersdorfer & Pratsinis, 2014; Walter et al., 2013).

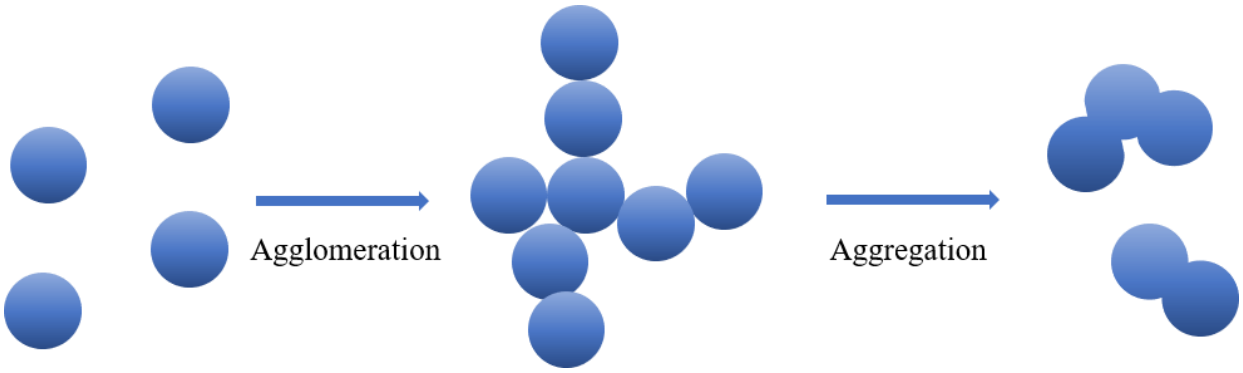

Figure 5.1 A schematic presentation of the formation of agglomerates and aggregates from monodisperse primary particles.

Particle size distributions

Nanoparticles from laser ablation has, according to Ullmann et al. (2002), a primary particle size distribution from 5 nm to 13 nm d_{mob} for materials such as aluminium, titanium, iron and silicon. Similar observations were made in laser-based additive manufacturing of steel, where the primary particles ranged between 4 nm to 16 nm geometric diameter (d_g) in size (Noskov

et al., 2020). Particles with a main peak concentration between 0.9-1.2 µm d_g and peak particle concentrations up to 700 particles/cm^3 were measured in aerosols generated from CO_2 laser cutting of 3 mm steel materials by Pena et al. (1998). More recent studies of particle size distribution from laser cutting and other laser-based methods by real-time spectrometry and SEM, show a mean size distribution ranging from 60-500 nm (Cai et al., 1998; Dazon et al., 2020; Elihn & Berg, 2009; Elihn et al., 2011).

Particle morphology

The most common particle morphologies in metal fume are spherical primary particles in agglomerates or aggregates and can be found in particles from laser-based additive manufacturing as well as welding (Antonini et al., 2006a; Jenkins & Eagar, 2005; Noskov et al., 2020; Sowards et al., 2010; Zeidler-Erdely et al., 2012). Larger spherical particles (100 nm – 1 µm) have occasionally been observed among the agglomerates (Antonini et al., 2006a; Wang et al., 2017). Fume particles containing Ti have also been observed as spherical particles in agglomerates (Cyr et al., 2000). Ultrafine particles found in aluminium smelter work environment been found to have variable shapes. In addition, to the chain like agglomerates, similar to what was observed in laser cutting and welding fume, has particles with a needle/fibre shape been found in (Thomassen et al., 2006).

Chemical composition

The elemental composition of fume particles reflects the origin, the main metal and the alloying elements (Pena et al., 1998). In addition, trace elements and coating components such as silver (Ag), gold (Au), chlorine (Cl), Cu, fluorine (F), potassium (K), Li, Mg, sodium (Na), phosphorous (P), lead (Pb), sulphur (S), Si, Sn, and Zn are found in various amounts in metal fume (Antonini et al., 2009; Oprya et al., 2012; Stanislawska et al., 2017). The primary mineral phases are oxides of the main alloying elements, determined through both gravimetric analysis and X-ray diffraction (XRD) (Cabanillas et al., 2005; Ullmann et al., 2002). Particles with a diameter >30 nm from laser-based additive manufacturing, had a metal core and an oxidized outer layer (Noskov et al., 2020). Complex phase compositions, with oxides in the form of spinel groups, had been found through XRD analysis of welding fume (Floros, 2018). Spinel structures have the general formula AB_2X_4 whereas A is usually a divalent cation, B is a trivalent cation and X a divalent anion, usually oxygen (Rayner-Canham & Overton, 2014). Elements that can easily adopt the cation state are Fe, Mg, Al, Cr, Ni, Mn, Cu, and other transition metals.

The solubility of the PM in the lung plays a role in the toxicity of the particles (McCarrick et al., 2019). Berlinger et. al. (2019b) investigated the bio-accessibility of elements from welding fumes using a simulating lung lining fluid. The solubility was highly variable with a median solubility < 1% for Al, Fe, Pb, Ti, between 4 and 6% for Cobalt (Co), Cr, Ni, V, and W, and between 13 and 27% for cadmium (Cd), Cu, Mn, and Zn. Both the welding techniques, production areas and the mineral phase of the particles had a significant effect on bio-accessibility. The water-soluble content was significantly higher in stainless steel compared to non-stainless steel fumes in a study comparing the total and soluble metal content from flux-cored arc welding fumes (Yoon et al., 2009). The solubility of the PM will not be determined in this study, but must be kept in mind in toxicity studies.

Chapter 6 Analytical methods

Particle diameter

Different particle sizing techniques report different "equivalent diameters", based upon particle properties (Kulkarni et al., 2011). Particle density and physical morphology play an important role in diameter measurements. Three common varieties are geometric diameter (d_g), aerodynamic diameter (d_{ae}), and mobility diameter (d_{mob}) linked to SEM, APS, and SMPS analysis respectively.

A spherical particle's d_g is simply the diameter of the sphere, but with nonspherical particles are their diameter generally characterized by an equivalent diameter. An equivalent diameter is defined as the diameter of a sphere that would yield the same size measurement as the particle under consideration (DeCarlo et al., 2004). The d_{ae} of a particle is defined as the diameter of that same particle if it was a sphere with the density of one, which settles in still air at the same velocity as the particle in question (Yassi et al., 2001). The motion of particles at nanometre size is however less dependent on inertia and d_{mob} is then used (Kulkarni et al., 2011). This diameter is based on an equivalent spherical particle with the same movement in a constant electric field (DeCarlo et al., 2004).

The d_{ae} is dependent on particle density, and therefore the particle composition. An increase in particle density will subsequently lead to an increase in d_{ae}. Spherical particles with a density >1 g/cm^3 will have a larger d_{ae} than their geometric diameter. Agglomeration and aggregation of primary particles affect the measurable diameters. The latter is because an irregular particle, e.g., agglomerate, will have the same trajectory in an electrical field as a spherical particle of a

greater volume (DeCarlo et al., 2004). With the increasing irregularity of a particle would the density of the particle degrease and subsequently the d_{ae} of the particle as well.

Real time particle number concentrations and size distribution

The Scanning mobility particle sizer (SMPS) is based on the principle of mobility of charged particles in an electrical field (Wang & Flagan, 1990). Particles go through a neutralizer before entering a differential mobility analyser (DMA) (Maricq et al., 2000). The neutralization does not neutralize all charge but brings the particles to a known charge distribution of negative and positive particles (Wiedensohler et al., 2012). The DMA is formed as a cylinder with a negatively charged rod at the center. Particles enter the DMA, and the charged particles move towards the central rod at a rate dependent on their electrical mobility (Knutson & Whitby, 1975). Particles with a given mobility exit at the top of the DMA and to a particle counter – like a condensation particle counter (CPC). Scanning of a broader particle size spectrum is possible by stepwise changing the voltage of the inner rod. The size fractionated particles go through to a CPC where alcohol or water condenses onto the particle. The particles then form droplets which can be detected based on light scattering (TSI, 2002).

While a SMPS can detect particles <500 nm in d_{mob}, can an Aerodynamic particle sizer (APS) able to detect particle sizes between 0.5 to 20 µm d_{ae}. The particle size is determined by *time-of-flight* as the time it takes for a particle to travel through an accelerating flow field (Peters & Leith, 2003). The APS accelerates the aerosol sample through an acceleration orifice where small particles reach a higher velocity than larger particles. The sample exits the orifice and enters the optic chamber for detection. The optic chamber contains two partially overlapping laser beams, where the particles pass through. An elliptical mirror collects scattered light onto a photodetector, that converts the light into electrical pulses. These pulses are then directly correlated with the particle velocity and thereby aerodynamic diameter (TSI, 2004).

Scanning electron microscope

In Scanning Electron Microscopy, electrons are used rather than light to create an image. It is possible to produce images with magnification up to 1,000,000 X, 1000 times greater than a typical light microscope (Tronsmo, 2016). This is achieved by using a high energy electron beam, which is produced in an electron gun by e.g., a heated Tungsten filament. The beam is then focused using condenser lenses and different apertures to create a thin beam. Coils are used to control the electron beam and to move it across the specimen surface in a raster pattern (Brandon & Kaplan, 2008; Goldstein et al., 2018). The high energy electrons react with the

sample and emit secondary electrons, backscatter electrons, X-rays and Auger electrons, which can be measured by different detectors (Skoog et al., 2018).

The sample is mounted inside of the sample chamber and both the electron beam column and sample chamber are kept with a certain amount of vacuum. The vacuum removes atoms from the air that would interfere with the electron beam. Detectors are placed in the sample chamber to detect the difference signals produced when the beam strikes the sample.

Secondary electron

Secondary electrons are emitted when the electron beam strikes the sample surface and dislodges an electron (Brandon & Kaplan, 2008). As these electrons are not from the original beam, the energy of these electrons is lower than the backscatter electrons. The secondary electrons are produced from the surface of the sample (Pepper et al., 2014), as the low energy electrons are easily absorbed within the sample. Thus, these electrons are localized to the point of impact and primarily provide information of the topography and morphology of the sample (Brandon & Kaplan, 2008).

Backscatter electron

Backscatter electrons are electrons from the initial electron beam that are reflected from the sample. These electrons collide elastically with an atom, changing the direction while the speed of the electron is almost unaffected. Thus, these electrons have an energy near the electron gun voltage (Skoog et al., 2018). The amount of backscatter electrons provides an indication of the atomic density of the sample, as more electrons will backscatter when striking a high-density material. The difference in density causes an atomic number contrast in the backscatter electron images. Particles with a higher density will appear lighter due to a higher signal (Goldstein et al., 2018).

Energy dispersive X-rays

The use of an EDX-detector provides the opportunity to examine the chemical composition of a sample (Skoog et al., 2018). The electron beam causes a generation of X-ray waves because elements will, when exposed to high energy electrons, absorb, and emit radiation with specific wavelengths (Skoog et al., 2014). These wavelengths are characteristic for each element. The relative elemental composition can be determined by knowing the specific emission voltages (keV) of an element and comparing the signal from different elements (Skoog et al., 2018). The qualitative identification and quantitative determination can be simplified by an analytical

software and standardless quantification (Goldstein et al., 2018). This detector will thereby give an indication of the chemical composition of single particles from specific materials, in comparison to ICP-MS analysis which provides selected element concentrations of bulk material.

P/B-ZAF is a standardless quantification method used for SEM-EDX and obtained by using variety of fundamental calibration methods. Instruments are characterised, and the fundamental parameters are stored within a database. Spectra can then be calculated by fundamental physical formulas in the atomic database. These are further matched with samples by iterative methods to estimate the concentration of analytes (Skoog et al., 2018). The P/B stands for the peak to background ratio, while ZAF act as a matrix correction. The ZAF correct for a difference in atomic number (Z), absorption of x-rays in the sample (A), and fluorescence yield from x-rays (F) where the x-rays themselves fluoresce more x-rays (Mehta, 2012).

Electron backscatter diffraction

Patterns from EBSD allow for crystallographic information of the specimen. Electrons are scattered in all directions, diffracted by crystal planes of the sample (Wilkinson & Britton, 2012). The diffracted electrons may escape the sample, and some will collide and excite a phosphorus screen, causing it to fluorescence. Patterns are then captured by a photosensitive imaging detector and analysed by software comparing the captured pattern with theoretical patterns of lattice structures (Michael & Goehner, 2001). The number of potential mineral phases is reduced by combining EBSD and EDX as the relative elemental composition is known.

Electron backscatter diffraction is normally applied to mineral phase identification on flat polished geological samples. However, studies have shown that that EBSD also can be applied to single particles (Bandli & Gunter, 2012; Ervik et al., 2018; Michael & Goehner, 2001; Small & Michael, 2001; Wilkinson & Britton, 2012)

ICP-MS

Inductively coupled plasma act as an ionizer and is linked to a mass spectrometer where the ionic mass is determined as mass per charge (m/z). The ICP-MS yields both qualitative and quantitative information of chemical composition of the PM.

Samples in solution are the most common sample type in ICP-MS analysis. The sample is introduced to the instrument by a sample introduction system consisting of a nebulizer to create

a fine aerosol and a gas chamber to remove larger droplets that can destabilize the plasma (Mora et al., 2003). Most used nebulizers are pneumatic, where the aerosol is formed by a high-speed gas jet over a tip of a small orifice (Linge & Jarvis, 2009). Introduction techniques such as spark, laser ablation, or glow discharge are used for solid samples (Skoog, Holler et al. 2018).

The plasma in the ICP torch is generated by argon gas in an alternating magnetic field made from a radiofrequency (RF) generator (Montaser, 1997). A spark introduces free electrons into the argon gas, resulting in ions and electrons. They are further accelerated by the RF field causing a chain reaction of ionization and forming a plasma with temperatures up to 10000 K (Boss & Fredeen, 1997).

A critical part of the instrument is the interface between the high temperature and atmospheric pressure of the ICP, to the low-pressure environment (10-4 torr) and room temperature mass spectrometer. It is accomplished through an ion transport system consisting of a sampling cone, skimmer cone and ion lenses. The hot plasma is transmitted through the sampling cone (water-cooled nickel cone with an orifice < 1.0 mm in the centre), forced by a reduction of pressure. An expansion of the argon gas containing the sample occurs and subsequentially cools it down. A fraction of the gas then passes through the second cone, the skimmer cone, to a chamber that is kept at the same pressure as the mass spectrometer. An ion lens system follows, where positive lenses focus the electron beam and negative lenses repel electrons and anions, prohibiting them from reaching the MS. The instrument may also include an off-axis system where ion lenses alternate the cations path, removing photons and neutral atoms and molecules (Skoog et al., 2018).

A commonly used mass spectrometer in ICP-MS is the quadrupole mass filter. A quadrupole consists of four metal rods applied radio frequency alternating current (RF-AC) and direct current (DC). A selected m/z passes through the quadrupole and all other ions will have an unstable trajectory and fail to meet the detector. Switching between m/z is rapid and data can be collected for the range of 0-300 amu in about 100 ms (Linge & Jarvis, 2009).

Multiple quadrupoles can be used in tandem to remove interferences. A reaction or collision cell will then be placed between two quadrupoles and gas can be applied. Helium (He) can be used as a collision gas as it will not react with the sample but affect the ions' kinetic energy. Bigger molecules will have reduced kinetic energy while atomic ions are unaffected. Molecules are then kept from entering the second quadrupole by a deflector with a constant voltage at the end of the reaction cell. The cell can be used as a reaction cell with for example O_2 or ammonia

(NH_3) gas. The gases can react with either the interference or the analyte causing a mass shift of +16 m/z, +32 m/z or +17 m/z(Skoog et al., 2018). Lastly, the cell can be used without a collision gas or reaction gas, and this mode is called No gas. This mode can be used on low mass ions with few interferences, where the signal would be disrupted by the presence of gas. A cautious selection of gas mode and analyte masses has to be made to optimise the analysis for each analyte.

A common detector in ICP-MS is the electron multiplier which is designed to collect and convert positive ions into an electric signal. The ion beam dislodged electrons from dynodes in a chain of successively higher voltage (Skoog et al., 2018). The signal is thereby multiplied and measured as electricity. The signal can be measured at two different locations in the detector, called pulse or analogue, ensuring a linear calibration curve over a large area (Skoog et al., 2018).

Interferences in ICP-MS

Isobaric interferences

Isobaric interferences occur when two atomic ions have the same mass and charge, for example $^{58}Ni^{+}$ and $^{58}Fe^{+}$. These interferences can be avoided by simply measuring at another isotope or corrected for by measuring the interference at another mass and removing the overlap from the analyte signal. There are isobaric interferences between multiple analytes, e.g., $^{64}Ni^{+}$ and $^{64}Zn^{+}$, $^{54}Cr^{+}$ and $^{54}Fe^{+}$, $^{204}Hg^{+}$ and $^{204}Pb^{+}$, especially as multiple analytes have close atomic numbers. A cautious selection of masses must hence be made.

Molecular interferences

Polyatomic complexes are generated in the cooler areas of the plasma and may cause interference with monoatomic ions (Montaser, 1997). A relevant example is $^{40}Ar^{17}O^{+}$ and $^{57}Fe^{+}$, but molecular interferences are common across most of the periodic table (May & Wiedmeyer, 1998). Molecular interferences can be avoided by analysing at another mass or by a reaction/collision cell when using a triple-quadrupole instrument. A cell filled with collision gas will remove polyatomic interferences based on kinetic energy, while a reaction gas alters the analyte or interference. Many metals, e.g., Fe, Cr, Ti, and Mg react to O_2 forming a mass shift of +16 z/m. Polyatomic interferes, however, does not react with oxygen and will not have a mass shift.

Double charged ions

Elements with a secondary ionization energy lower than the first ionization energy of argon will form double charged cations. These ions will possibly interfere with single charge ions with half the mass. $^{136}Ba^{2+}$ is a common interference for $^{68}Zn^{+}$ as Barium can form Ba^{2+} in the plasma. This type of interference can be avoided by choosing another mass or optimizing the instrument through a reaction cell.

Matrix interferences

The ionization effect of the plasma can be reduced if the matrix contains high concentrations of easily ionized atoms (Skoog et al., 2018). This interference might be reduced by dilution or by removing the easily ionized elements.

Solutions with a heavy matrix component, e.g. uranium (U), Pb and bismuth (Bi), or a solution with a generally high number of ions present, will be affected by the space charge effect (Skoog et al., 2018). The space charge effect is the mutual repulsion of ions within the ion beam when the density of ions are high enough for them to interact with each other (Montaser, 1997). The lower mass ions have a lower linear momentum and will therefore be more easily deflected than heavier ions. This might lead to a mass bias reducing the transmission of lighter ions as these are "pushed out" of the ion beam and the signal intensity of low masses decreases (Skoog et al., 2018). Space charge effect can cause an issue when analysing for low mass elements such as Li in a sample matrix containing heavier elements. A solution may be to dilute the samples.

Chapter 7 Method and materials

Sampling

Samples of metal fume and dust particles were collected from three different production sites. At each site, plates of aluminium, titanium, or different steel qualities were processed by means of different types of laser-cutters. An enclosed Bystronic fiber-laser (Bystronic Laser AG, Niederönz, Switzerland) was used to cut three different thicknesses of stainless steel plates (5, 6, and 15 mm) with oxygen as assistant gas. In addition, two black-steel plates (3 and 3.2 mm) were cut with nitrogen as assistant gas. The other three lasers were CO_2- lasers. Acid-proof (3 mm), cold-treated (2 mm), heat-treated (3 mm), and oil-coated steel plates (1.5 mm), as well as an aluminium (0.5 mm) and a titanium plate (4 mm) were cut by an enclosed Trulaser 5030 Classic 5kw (TRUMPF, Singapore). A partially build-in C 4400W power Bystronic Bystar (Bystronic Laser AG, Niederönz, Switzerland) laser was used to cut aluminium plates (10 mm).

At the same site, an open Bystronic Byflex laser (Bystronic Laser AG, Niederönz, Switzerland), was used to cut black steel plates coated with a teflon layer (2.3 mm). Aluminium-based plates were processed at the beginning of the shift, and the teflon coated black steel was cut in parallel for the last 1 hour and 40 minutes. A full representation of materials is presented in Table 7.1

Table 7.1 The different metal plates processed at the three different production sites.

Material	Characteristics		Comments
	Thickness (mm)	Laser type	
Acid-proof steel	3	CO_2	N_2 as assistant gas
Aluminium	0.5	CO_2	
Aluminium	10	CO_2	
Black steel	3 and 3.2	Fiber	N_2 as assistant gas
Black steel	2.3	CO_2	Steel covered coated with a teflon layer on one side
Stainless steel	6	Fiber	O_2 as assistant gas
Stainless steel	15	Fiber	O_2 as assistant gas
Stainless steel	5	Fiber	O_2 as assistant gas
Steel	1.5	CO_2	Cold rolled, covered with carbon-based oil
Steel	3	CO_2	Heat rolled, with carbon-based oil
Steel	2	CO_2	Cold rolled
Titanium plate	4	CO_2	

Exposure limits

The exposure assessment of the laser cutting industry involves the main alloy elements in the metal plates cut, in addition to possible impurities in the material, discussed in subchapter about laser-cutting materials, see Table. 7.1. The OEL's for the exposure assessment are obtained from the ATIL, see Table. 7.2 (Norwegian Ministry of Labour and Social affairs, 2013). The most relevant OEL will be used when there is no directly comparable limit.

Table 7.2 List of occupational exposure limits for work atmosphere based on the Norwegian labour inspection authority (Norwegian Ministry of Labour and Social affairs, 2013).

Element	Comments	OEL (mg/m^3)
Aluminium	Aluminium from welding fume	5
Cadmium	Cadmium oxides	0.02
Chromium	Cr^{2+}- and Cr^{3+} complexes	0.5
Copper	Smoke	0.1
Iron	Iron oxide	3
Lead	Lead and inorganic lead complexes in smoke, fume, and dust	0.05
Magnesium	Magnesium oxide	10
Manganese	Manganese and inorganic manganese compounds - respirable fraction	0.05
Mercury	Mercury and mercury compounds	0.02
Molybdenum	Insoluble	10
Nickel	Nickel and nickel compounds	0.05
Silver	Silver, metal dust and fume	0.1
Tin	Inorganic compounds	2
Titanium	Titanium dioxide	5
Tungsten	Soluble	1
Vanadium	Smoke	0.05
Zinc	Respirable fraction	5

Collection of respirable dust for exposure assessment

Respirable particles were sampled in the breathing zone of a total of five workers in three different production sites. Two parallel samples were collected per worker. The PM was collected with Higgins-Dewell (JS Holdings, UK) cyclones onto 37 mm 5.0 µm pore-sized polyvinyl chloride filters (PVC) (Millipore Corp., Billerica, MA, USA). A GSA SG5200 pump (Ratingen, Germany) was used to pump air through the filters. The pumps were calibrated to an airflow of 2.2 L/min prior to sampling with a rotameter (Aalborg Instruments & Controls, Inc, New York, USA). The airflow was measured again with the same rotameter after sampling and potential flow changes were corrected for in-data processing. Additionally, two stationary

respirable cyclones were placed in the working hall at one of the sites, mounted at approximately one meter's height.

Real-time particle number and size measurements

Two different real time spectrometers were used to measure airborne particle concentrations. The number of airborne particles from 0.5 to 20 µm d_{ae} was measured by a TSI Incorporated 3321 Aerodynamic Particle Sizer (APS) (Shoreview MN, USA). Airborne particle concentrations from 11.3 to 461.1 d_{mob} nm for fiber-laser and 30.0 to 615.3 nm d_{mob} for CO_2-laser was measured by a TSI Incorporated Scanning Mobility Particle Sizer (SMPS) (Shoreview MN, USA) equipped with an Electrostatic Classifier (Model 3082), a Long Differential Mobility Analyzers (DMA) (Model 3081A) and an Ultrafine Condensation Particle Counter (CPC, Model 3756). Each sampling cycle, measuring the mentioned diameters, lasted one minute and 20 seconds.

The SMPS inlet was extended with a polytetrafluoroethylene (PTFE) tube (TSI Incorporated, Shoreview, MN, USA) of approximately two-meter length at two of the sites with enclosed lasers. The extended SMPS inlet was placed inside the cover of the laser-cutter. This was not applicable at the third production site as two lasers were used simultaneously on different materials. The SMPS inlet was then placed between the two laser cutters, approximately 1 meter from each. The inlet for APS inlet was placed outside of the laser chamber in all cases, measuring the concentration of particles in the workplace atmosphere.

Collection of particles for SEM analysis

Particles were collected onto copper TEM grids with holey carbon films (Holey Carbon film on Copper H7, Agar Scientific, Stansted, UK). The 5 mm grids were fixed in the middle of 25 mm PVC filters (Millipore Corp., Billerica, MA, USA) and placed within closed face aerosol plastic cassettes (Millipore Corp., Billerica, MA, USA). Sampling was done inside the laser chamber using in-house built PS103 model sampling pumps (National Institute of Occupational Health, Oslo, Norway). The filters were exposed in the range from 1 minute up to 11 minutes and 30 seconds. Three filters with particles were collected with increasing exposure time per plate material cut, to have multiple options to choose from as an overload of particles can occur.

Collection of PM from specific materials for ICP-MS analysis

Total dust was collected onto Millipore 25mm 5.0 µm pore-size PVC membrane filters (Millipore Corp., Billerica, MA, USA) placed in closed face "total" aerosol plastic cassettes (Millipore Corp., Billerica, MA, USA). The cassettes were connected to in-house built PS103

pumps (National Institute of Occupational Health, Oslo, Norway). The pumps had a calibrated airflow of 2 L/min. The PM were collected inside the cover of the laser cutters. Seven parallels were made per sampling cycles, one dedicated for elemental composition by ICP-MS and six dedicated to mineral phase determination with XRD.

The two fully enclosed lasers had ventilation systems, where the dust was collected into large buckets. Particulate matter from the buckets ($PM_{ventilation}$) was transferred into 15 mL polypropylene centrifuge tube (Sarstedt, Nümbrecht, Germany) for determination of total chemistry by ICP-MS

Analysis

Overview

Several different samples were taken at different production sites as described in the subchapters above. The analytical method and purpose of each of these are summarized in Table. 7.3.

Table 7.3 A summary of sample type, analytical technique and the information obtained.

Sample names	Collected	Analytical technique	Information
Respirable cyclones	Stationary or personal	ICP-MS	For exposure assessment
Airborne particles **APS** **SMPS**	 Outside laser chamber Inside laser chamber	Real time spectrometers	APS -size distribution of all particles outside of the laser-cutter. SMPS - size distribution of particles from specific materials. For exposure assessment and comparing to SEM images.
Particles from specific materials	Inside laser chamber	SEM-EDS	High resolution images for particle morphology and size distribution to compare with SMPS
	Inside laser chamber	SEM-EDS	Chemical composition to compare with PM samples analysed by ICP-MS.
	Inside laser chamber	SEM-EBSD	Give an indication of mineral phase in selected particles.
	Inside laser chamber	ICP-MS	Bulk composition of particles from specific materials
$PM_{ventilation}$	Ventilation system	ICP-MS	Compare with PM from specific materials.

Gravimetric analysis

All filters were conditioned in a controlled environment with relative humidity of 40% ± 2% and temperature of 20°C ± 1°C for at least 24 hours before weighing. The filters were then weighed on a Sartorius semi-micro model MC5 balance (Sartorius AG, Göttingen, Germany) before sampling. All samples were conditioned in the same weighing room after the sampling for at least 24 hours, before being weighed using the same balance.

The balance was checked by weighing different weights and a reference filter with known masses prior to the gravimetrical analysis. Unexposed filters (blind filters) were used for correction and weighted at the same time as the samples. All filters were discharged by a radioactive source.

Operator-controlled scanning electron microscope analysis

Particles were analysed by means of a Hitachi SU6600 field emission SEM (Hitachi, Tokyo, Japan), equipped with a Bruker energy dispersive X-ray (EDX) detector (Bruker Nano GmbH, Berlin, Germany) and a NORDIF electron diffraction backscatter (EBSD) detector (NORDIF, Trondheim, Norway). Scanning electron microscope was used for three different purposes: morphology, chemical composition by EDX, and mineral phase information by EBSD.

Morphology by high resolution SEM

Samples from the same material with different exposure times were investigated to obtain an overview of particle morphology and sample load. High resolution images were collected from the selected samples using the settings presented in Table 7.4. Two overview images were taken of different areas of each sample with a ~ 5000x to ~10 000x magnification in addition to higher magnification images of particles.

Table 7.4 SEM Instrument settings used for overview imaging.

Instrument settings	
Acceleration voltage (electron beam)	30 keV
Extraction voltage	1.9 kV
Suppressor voltage	300 V
Probe current	High Resolution
Working distance	10 mm
Sample tilt	0˚

Qualitative particle analysis by SEM-EDX

Chemical composition of particles was determined by EDX. An acceleration voltage of 20 keV was applied to detect possible Pb particles. A medium probe current was applied to minimize the signal to noise ratio in EDX spectrums, see Table 7.5 for more instrument settings.

Agglomerates and aggregates with primary particles greater than 50 nm d_g were analysed by point analysis, focusing the beam on one single point on a primary particle. An area function was used when no signal could be obtained by point analysis, due to agglomerates/aggregates with primary particles <50 nm d_g, drift, or with overloaded samples with no clear distinction between particles. The presence of elements within the defined circle with approximate diameter of 100 nm – 200 nm were analysed in the aggregate/agglomerate. The number of scans depended on the loading of the sample, where ~40 scans were made if the sample had an overloaded with great stacking of particles and ~50-60 scans were made when analysing distinguishable particles. A new image of the analysed area was taken after every fifth scan to correct for drift in the electron microscope.

Table 7.5 SEM Instrument settings used for particle chemistry analysis by EDX.

Instrument settings	
Acceleration voltage (electron beam)	20 keV
Extraction voltage	1.9 kV
Suppressor voltage	300 V
Probe current	Medium
Working distance	10 mm
Sample tilt	0˚
Scan time	20 sec

Bruker Quantax Espirt 1.4.5. software (Bruker Nano GmbH, Berlin, Germany) was used for EDX analysis. The particles were analysed with respect to a pre-set list of elements and standardless automatic detection P/B-ZAF. Automatic selection of elements was used to include elements that were not in the pre-set list. All spectrums were manually examined by the operator.

Certified reference material for ICP-MS analysis SSWF-1 Stainless steel welding fume (Health and Safety Executive, Buxton, UK) and MSWF-1 Mild steel welding fume (Health and Safety Executive, Buxton, UK) was transferred to TEM-grids for analysis by EDX. The specific

material was pumped onto TEM-grids placed in plastic cassettes by suction from an Oil-less diaphragm-type vacuum pump (Gast™, Benton Harbor, MI, USA).

Mineral phase by SEM-EBSD

Determination of the chemical composition of particles by SEM-EDX was made prior to EBSD analysis. This information was then used to reduce the number of possible mineral phases through EBSD analysis. The electron beam was controlled in spot mode to find an "optimal position" on the particle to obtain an electron backscatter pattern (EBSP). The EBSP was then loaded into the NORDIF software for band identification. Bands were detected and a voting scheme was used to identify the most probable index solution. A confidence index, with a range from 0 to 1, was calculated based on the voting scheme. This value indicated the accuracy of the simulated patterns. The mineral orientation with the most votes was then considered correct (Ervik et al., 2018). The same method as described in Ervik et al. (2018) will be attempted on particles from different materials to give an indication of mineral phase, see Table 7.6 for instrument settings.

Table 7.6 SEM Instrument settings used for EBSD analysis.

Instrument settings	
Acceleration voltage (electron beam)	20 keV
Extraction voltage	1.9 kV
Suppressor voltage	300 V
Probe current	High or Medium
Working distance	25 mm
Sample tilt	70˚

ICP-MS

Sample preparation including decomposition for ICP-MS

One of the two respirable cyclones from each worker was used for element analysis. Furthermore, one out of the seven specific material PM samples was chosen for elemental analysis. The filters containing the collected PM were carefully moved from the "total" cassettes and cyclones with tweezers and transferred into the decomposition vessels.

About 1.00 mg of $PM_{ventilation}$ from Production site 1 and 2 was weighed in on 25 mm PVC filters (Millipore Corp., Billerica, MA, USA) on an analytical weight (Sartorius AG, Göttingen, Germany). One sample was made of $PM_{ventilation}$ from production site 1 and three samples of

$PM_{ventuilation}$ were made from production site 2. Only one sample was prepared from production site 1 due to a shortage of raw material. The weighed filters with PM were then transferred into separate decomposition vessels.

About 1.00 mg of the SSWF-1 Stainless steel welding fume (Health and Safety Executive, Buxton, UK), MSWF-1 Mild steel welding fume (Health and Safety Executive, Buxton, UK) and SRM 1880b – Portland Cement (National institute of Standards and Technology, Gaithersburg, USA) was weight in on an analytical weight (Sartorius AG, Göttingen, Germany). Three parallels were made from the steel reference materials and one parallel of cement. One Portland cement sample was prepared due to a limitation in number of decomposition vessels. Portland Cement had a less similar matrix compared with the samples, as the main components were silicates. All CRM were weighed in on 25 mm PVC filters (Millipore Corp., Billerica, MA, USA) and transferred into separate decomposition vessels (Milestone, Fatebenefratelli, Italy).

Six field blanks for specific material PM and six respirable cyclone blanks were made in addition to eight filter blanks from 25 mm PVC filters (Millipore Corp., Billerica, MA, USA) and eight method blanks. All blanks were treated as the samples.

A portion of 2.00 mL of an acid mix containing 1.95 mL aqua regia (1:3 HNO_3 and HCl) and 0.05 mL HF 48% (w/w) were added to the decomposition vessels. The mix was made from 65% (w/w) HNO_3 (Sigma-Aldrich, Merck KGaA, Darmstadt, Germany), 37% (w/w) HCl (Sigma-Aldrich, Merck KGaA, Darmstadt, Germany) and HF 48% (w/w) (Sigma-Aldrich, Merck KGaA, Darmstadt, Germany). A rhodium (^{103}Rh) standard was used as an internal standard for decomposition and 200 µL was added to the samples after the addition of acid. The containers were then closed carefully and placed in the Milestone MLS 1200 digestion module (Fatebenefratelli, Italy). The samples were decomposed in three cycles of 20 minutes (15 minutes at 250 W followed by 500 W for 5 minutes). All vessels were carefully rocked after the first cycle to ensure that all the samples were covered in the acid mix. The samples were then cooled down to room temperature.

The cooled samples were diluted to 15 mL with Milli-Q® water, before being transferred into 50 mL polypropylene centrifuge tubes (Sarstedt, Nümbrecht, Germany). The samples were then added 200 µL of a selenium (^{74}Se) and bismuth (^{209}Bi) standard for drift control of the ICP-MS analysis.

To make up for missing elements in the steel and cement CRMs, a CRM for elements in surface waters (SPS-SW2) was included. SPS-SW2 were diluted ten times in a 50 mL polypropylene centrifuge tube (Sarstedt, Nümbrecht, Germany) with internal standard and acid matrix as the samples.

All reagents used in sample preparation and analysis had a quality of pro analysis or purer.

Analysis

An Agilent 8800 QQQ ICP-MS with an Agilent Technologies SPS 4 Autosampler (Santa Clara, CA, USA) was used for elemental analysis. A tuning solution containing 1 µg/L Li, Mg, Co, yttrium (Y), Caesium (Cs), and thallium (Th) (Agilent Technologies, Santa Clara, CA, USA) with the same acid matrix as the samples was used to tune the instrument. All carrier solution had the same acid concentration as the samples and the wash solution contained 2% (V/V) aqua regia solution.

The samples were analysed for total element concentration of the following elements: Ag, Al, Cd, Cr, Cs, Cu, Fe, mercury (Hg), Li, Mg, Mn, Mo, Ni, Pb, S, Si, Sn, Ti, V, W, and Zn. The instrument was calibrated using a mixed standard solution with three levels of dilution dependent on the expected concentration of the sample. Main alloy elements that were of high concentration in the CRM were Cr, Fe, Mn, Ni, Si, Si and Zn. These analytes had an additional high concentration standardisation level to ensure linearity. All standards used were certified from Spectrapure Standards AS, Oslo, Norway.

Three different gas modes; O_2, He and no gas were applied. The elements measured with O_2 without mass shift were Ag, Cd, Cs, Cu, Hg, Ni, and Pb. Analytes detected with a mass shift were Cr, Fe, Mg, Mn, Mo, S, Si, Ti, V, and W. Aluminium, Mg, and Li were detected at no gas mode, while He was used to detect Sn and Zn. A full presentation of all analysed mass shifts and gas modes per analytes are found in Supplement 2, Table S2.1.

Method validation

Reference materials for stainless steel welding fume and mild steel welding fume were used as it represents a major part of the samples analysed. The NIST CRM Portland Cement reference material was included as the other two CRM does not include Ti and Al. The reference material SPS-SW2 – elements in surface waters will give an indication of instrument accuracy only.

The blanks were used to calculate the limit of detection (LOD) and limit of quantification (LOQ), defined as three and ten times the variation of blank samples, respectively.

Results for analysis of CRM are in Table S1.1-S1.3, in Supplement 1. Included are the percentage differences in measured and certified true values (BIAS). The BIAS act as a measure of the method accuracy, and the BIAS was required to be ≤25%.

Data processing

Two data processing programs were used for the treatment of data and graphical presentations, Microsoft Office Excel 2016 (Microsoft Corporation, Redmond, WA, USA) and R with RStudio integrated development environment (R core Team, 2018). The 'tidyverse' collection of R packages (Wickman et al., 2019) was used in Rstudio for particle size distribution plots and barplots and included packages such as 'ggplot2', 'dplyr', and 'tidyr'. Furthermore, the package 'ggtern', an extension to 'ggplot2' was used to produce ternary plots (Hamilton & Ferry, 2018).

Chapter 8 Results

Respirable dust

Particulate matter from personal carried respirable cyclones were analysed by ICP-MS and presented in Table 8.1 together with 20 % of relevant OEL's. The element concentration in air varied greatly within the defined SEG of laser cutter workers. Lead showed a median value 1000 times lower than the maximum concentration of 0.0068 mg/m^3. Chromium, Hg, Mo, Ni, V and W were quantified with maximum values below 0.0001 mg/m^3 is not included in Table 8.1 as the values are substantially below the OELV's. Cadmium concentrations were below LOD in all but one respirable dust sample.

Table 8.1 Selected element in PM collected for a SEG of five workers using respirable cyclones. All values are normalised to an 8-hour shift (480 min).

	Al	Cu	Fe	Mg	Mn	Pb	Sn	Ti	Zn
Min (mg/m^3)	0.00046	0.000014	0.0012	0.000044	0.000011	0.0000015	<LOD*	0.0000037	<LOD**
Median (mg/m^3)	0.0019	0.000030	0.0045	0.00010	0.000077	0.0000068	0.0000011	0.00011	0.0036
Max (mg/m^3)	0.0020	0.013	0.0078	0.00096	0.00016	0.0068	0.0021	0.0026	0.0041
20% of OEL (mg/m^3)	1	0.02	0.6	2	0.01	0.01	0.4	1	1

*0.0000010 (mg/m^3)

**0.00011 (mg/m^3)

Single particle characterisation

Particles (0.5 to 20 µm) measured by APS outside of the laser cutters had similar size distribution in all production sites, see Figure 8.1. The distribution had a d_{ae} from 0.5 µm to 2 µm, and peak concentrations at approximately 0.9 µm.

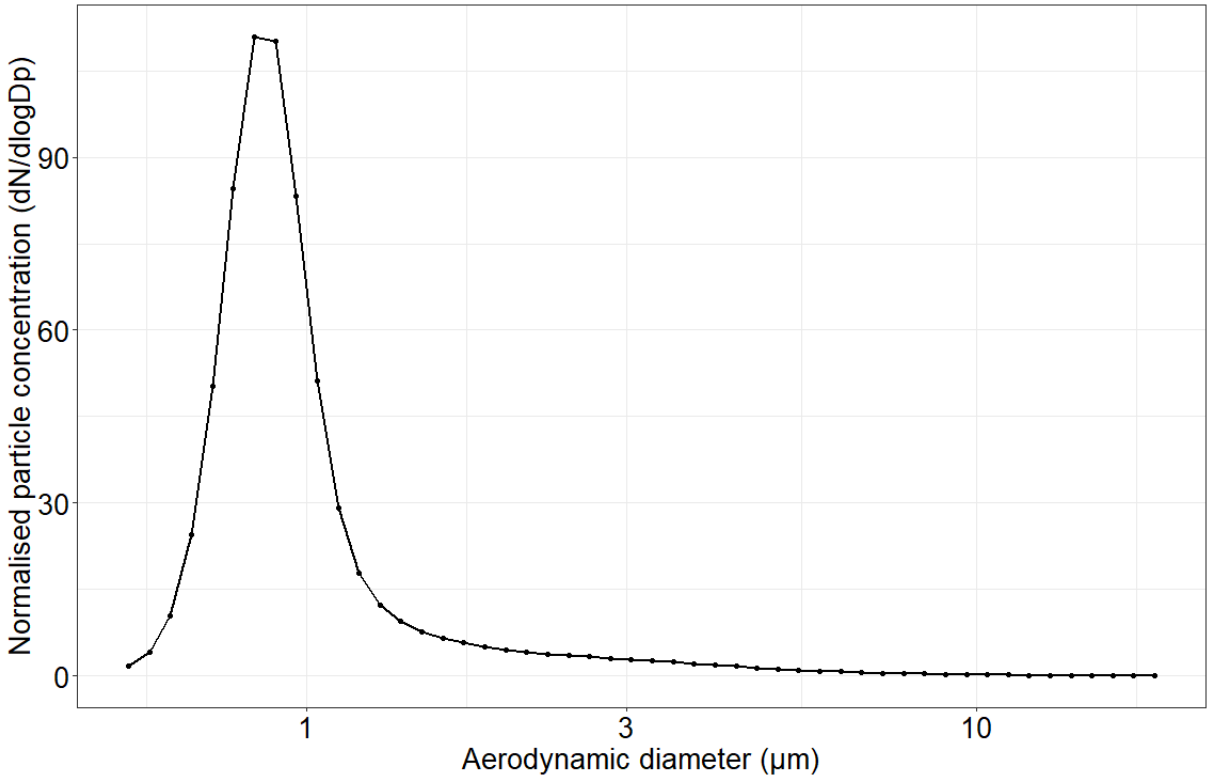

Figure 8.1 Average concentration of particles from laser cutting as a function of d_{ae}. Measurements were made in the work environment outside the laser cutter.

The inlet for SMPS measurements from cutting 10 mm aluminium-based plates and 2.3 mm steel with Teflon coating, see Figure 8.2, were measured next to the APS outside of the laser cutter. As expected, the particle concentration increases when the two open laser-cutters are used simultaneously. The size distribution shows particles with a d_{mob} mainly below 100 nm, in a range from 30 to 300 nm d_{mob}.

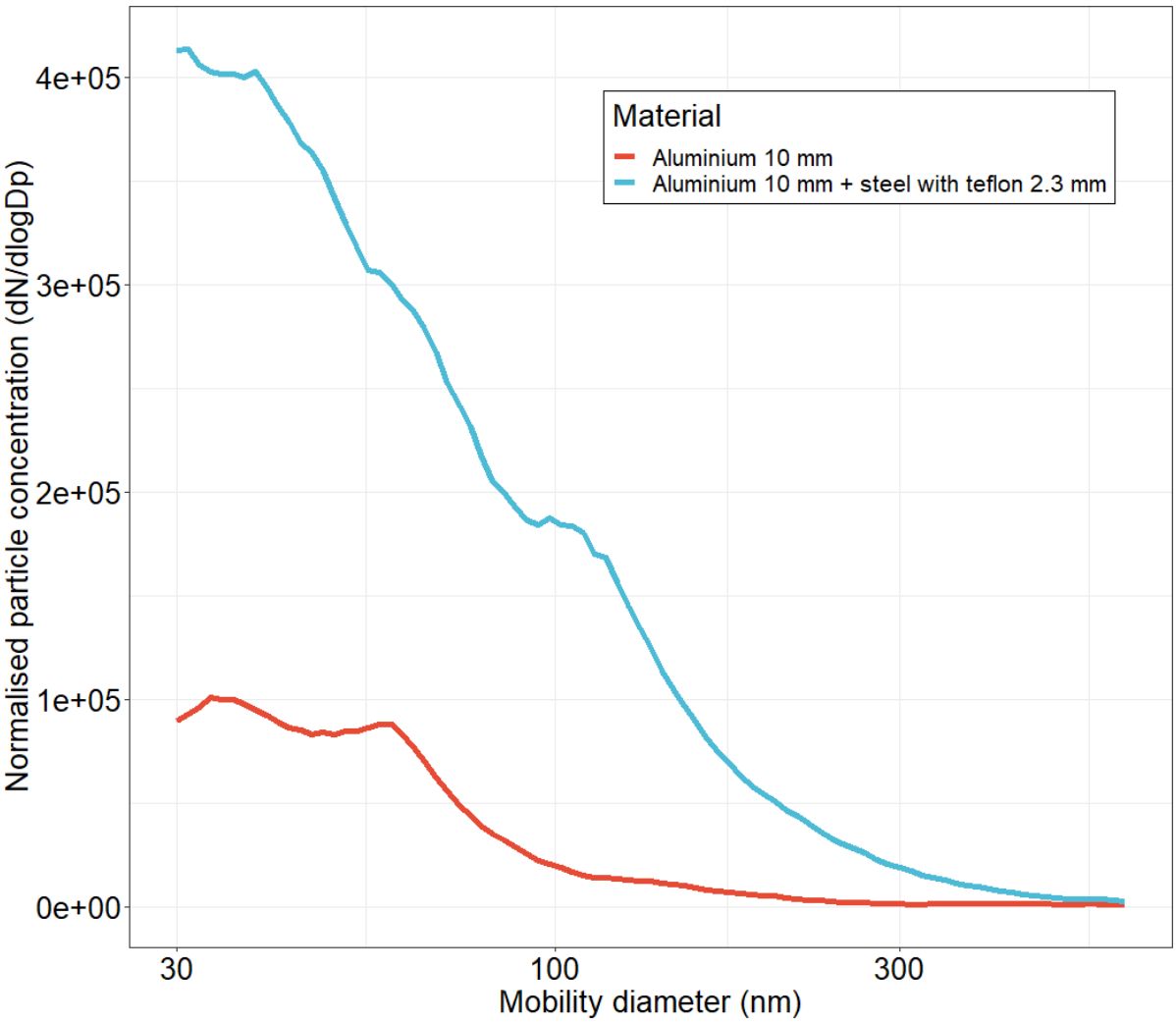

Figure 8.2 Average concentrations of particles from laser cutting aluminium-based plates by CO_2-laser, as a function of d_{mob}. The measurements were made by SMPS with an inlet outside of the laser cutter.

Titanium-rich particles

The particles emitted during cutting the Ti-based plate had the highest particle number concentration compared to all other samples collected. The highest concentrations were approximately 110 nm d_{mob}, and most particles had a d_{mob} between 50 and 350 nm, see Figure 8.3a. Titanium rich particles showed a tendency to agglomerate or aggregate. Some larger spherical particles were observed (>400 nm d_g) as seen in Figure 8.3b, but most primary particles showed a d_g of ~50 nm or lower.

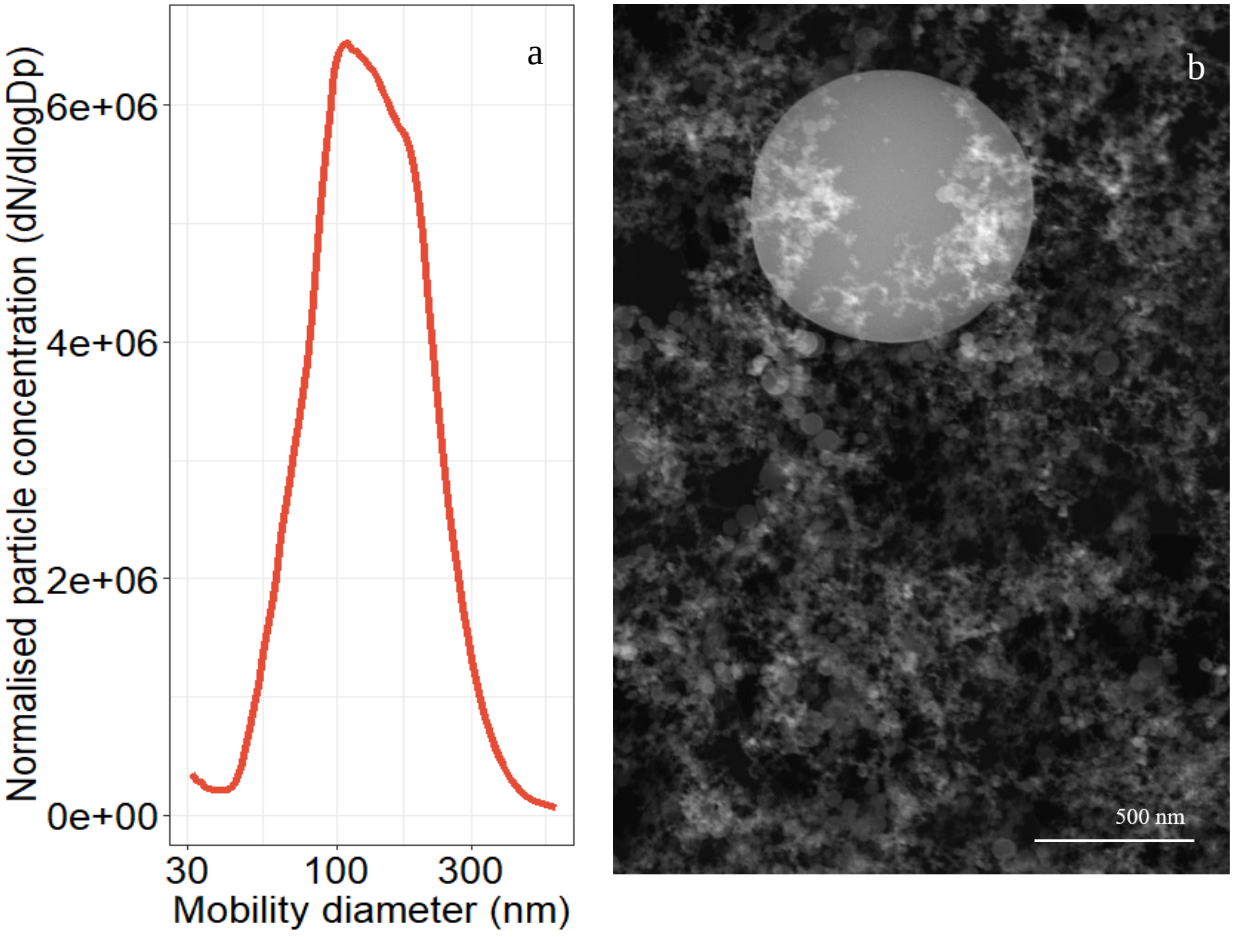

Figure 8.3 Average concentrations of particles from laser cutting a titanium-based plate by CO_2-laser, as a function of d_{mob} (a), with corresponding secondary electron image of typical titanium-rich particles (b).

Aluminium-rich particles

The particle size distribution from the Al-based plate had a bimodal shape with the two maximum concentrations around 95 nm and 235 nm, as seen in Figure 8.4a. The measured particle size distribution was from 55 to 615 nm d_{mob}. Aluminium-rich particles were found as agglomerates/aggregates of different sized primary particles from ~10 nm in d_g up to ~ 250 nm d_g in Figure 8.4b and 8.4c in samples from both 0.5 mm and 10 mm aluminium plates. Primary particles with a d_g below 50 nm were most common. The size of the agglomerates/aggregates ranged from ~100 nm d_g and up to a few micrometres, but only distinguishable in the 10 mm aluminium sample, as the 0.5 mm aluminium filter was overloaded with particles, see supplement 5, Figure S5.1.

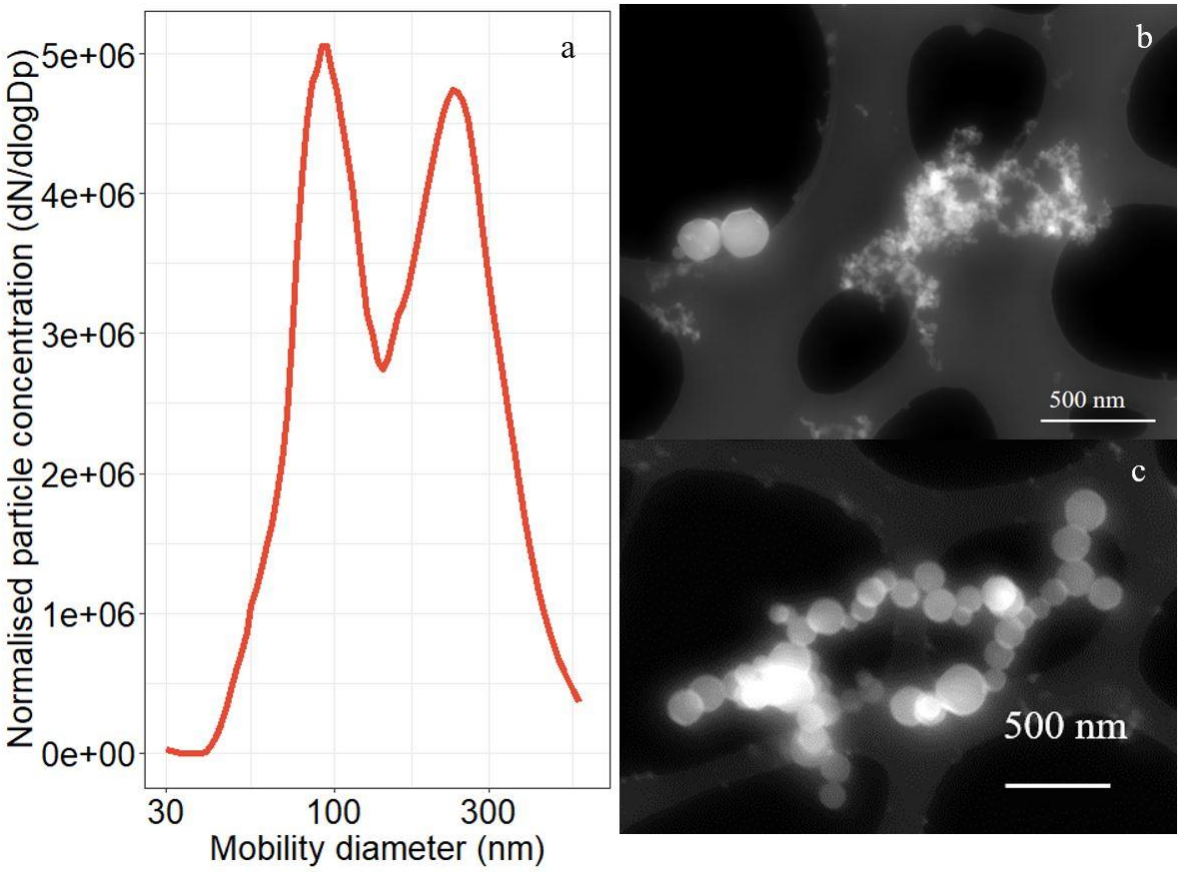

Figure 8.4 Average concentrations of particles from laser cutting a 0.5 mm aluminium-based plate by CO_2-laser as a function of d_{mob} (a), with secondary electron image of aluminium-rich particles (b and c) from 10 mm Aluminium-based plates.

Steel particles

Two different size distributions, one for each material type (stainless and black steel), were observed in the SMPS data from cutting with fiber-laser, see Figure 8.5. Stainless steel particles had a main size distribution ranging from 20 nm to 200 nm, with increasing particle concentrations with decreasing plate thickness. The highest concentrations were measured for particles with d_{mob} around 45 nm. Black steel had a size distribution from 15 to 460 nm d_{mob}, with the highest peak concentration around 100 nm d_{mob}.

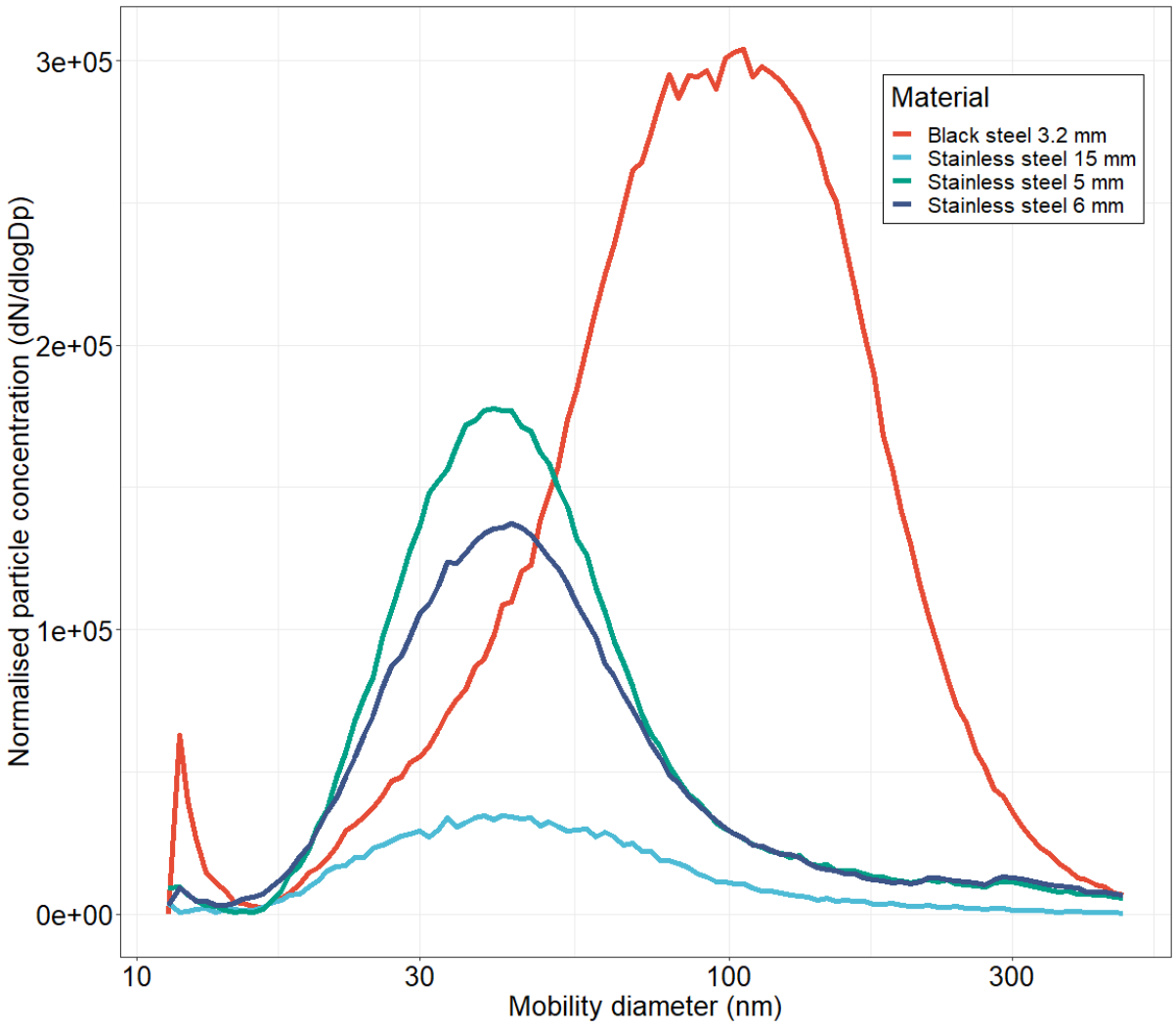

Figure 8.5 Average concentrations of particles as a function of d_{mob} from laser cutting different steel plates using a fiber-laser.

The lowest particle concentrations were measured when cutting 1.5 mm steel plates, with a maximum particle concentration of less than 1.0 x 10^5 particles/cm^3. Cutting acid-proof steel yielded the highest number concentration of all steel samples with a peak concentration of 2.8 x 10^6 particles/cm^3 of 78 nm and with main particles size ranging from 30 to 300 nm d_{mob}. The two steel plates, with different thicknesses presented in Figure 8.6, had d_{mob} at the main maximum peak concentration, 105 and 146 nm for 3 mm and 1.5 mm, respectively. Cutting 1.5 mm steel yielded main particle sizes in a broader span from 40 nm to 500 nm, while cutting 3 mm steel resulted in main particle sizes between 70 nm to 350 nm.

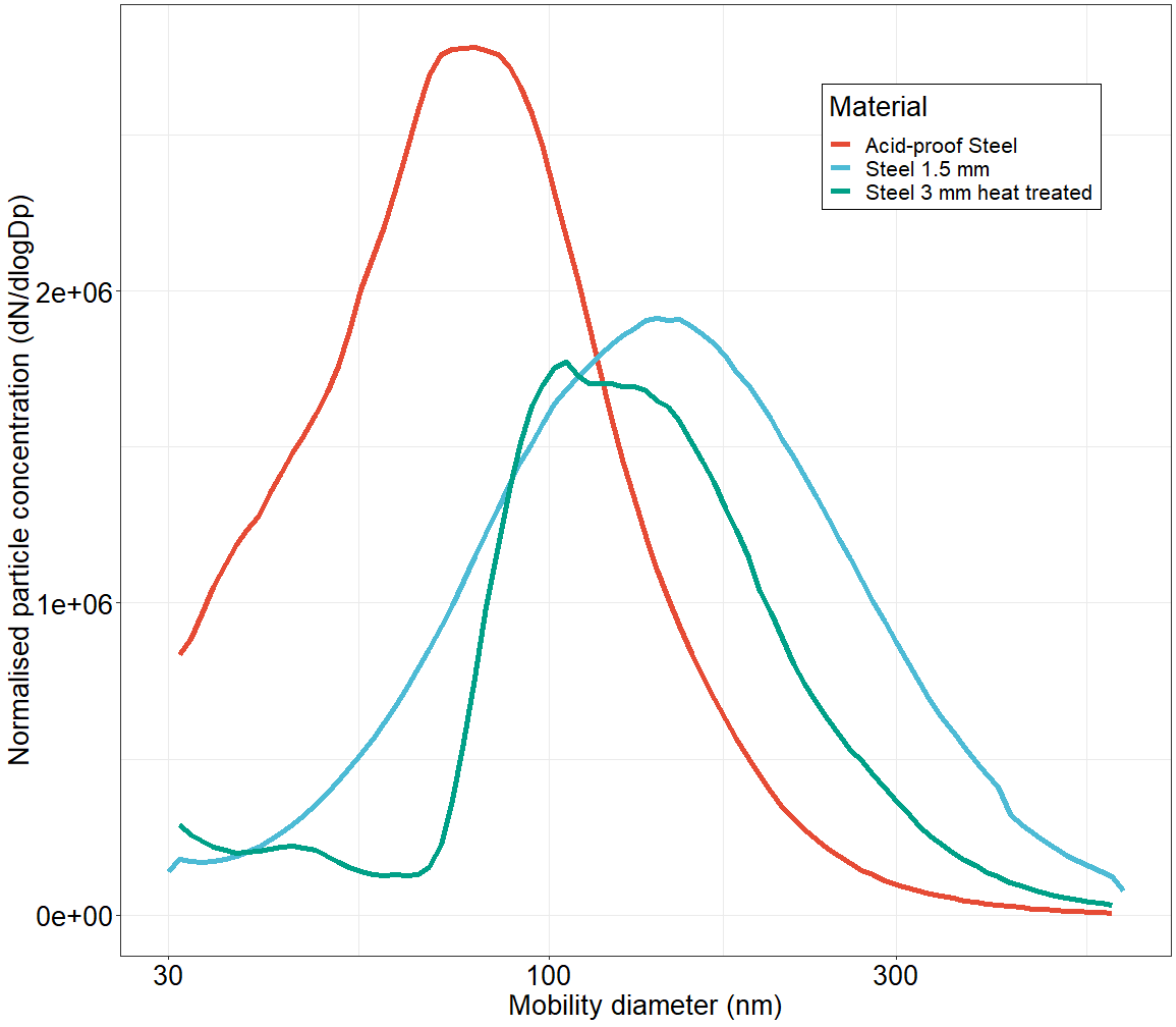

Figure 8.6 Average concentrations of particles from laser cutting selected steel plates by CO_2-laser, as a function of d_{mob}.

Particles collected during laser cutting of different thicknesses of steel, see Table 7.1, were analysed by SEM. Consistent for all samples, were chain like agglomerates/aggregates, see Figure 8.7 and Figure 8.8, with a d_g from 100 nm to 5 µm. Primary particles with a d_g of ~10 nm can be distinguished in Figure 8.8. The number of primary particles in agglomerates vary from two to hundreds of particles as seen in in Figure 8.9.

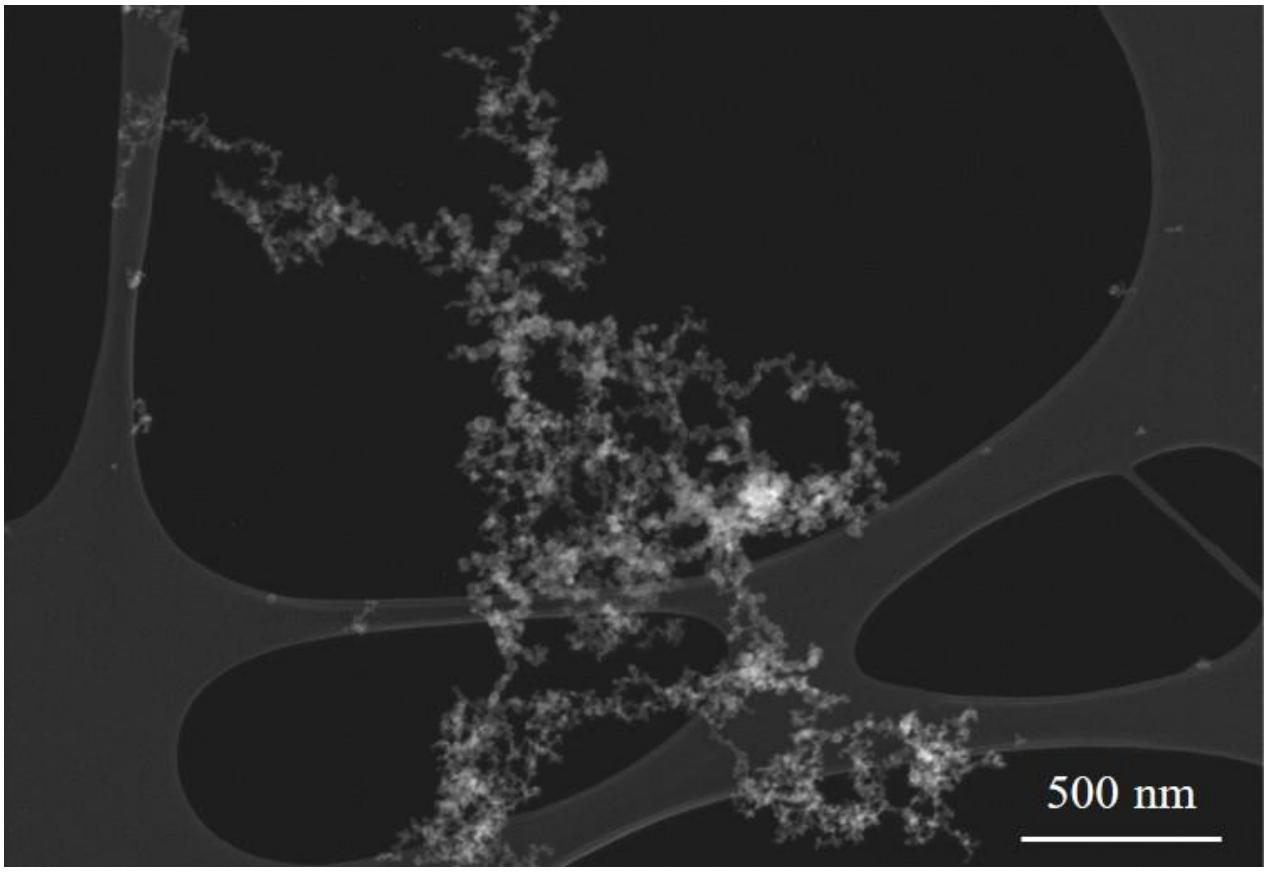

Figure 8.7 Secondary electron image of agglomerates/aggregates formed through laser cutting 6 mm stainless steel plates

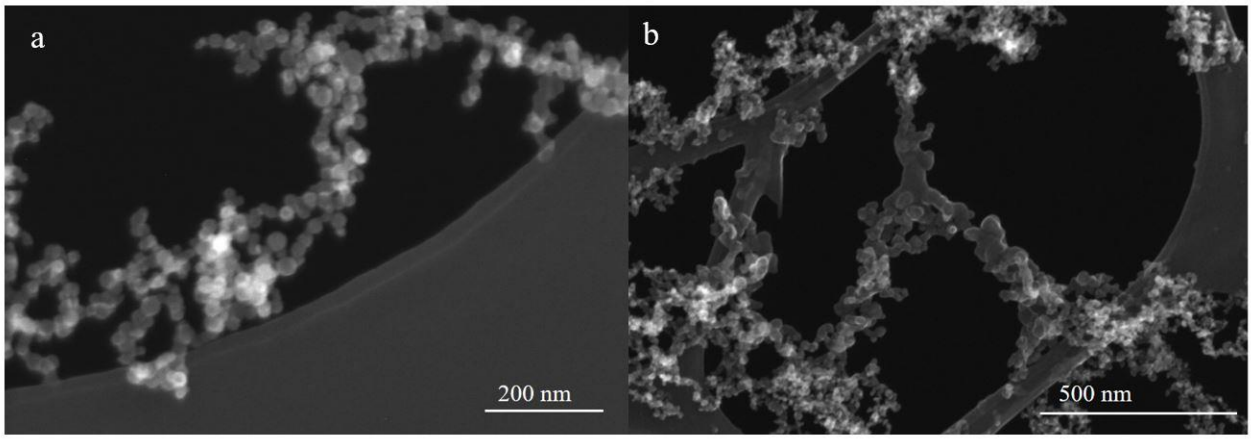

Figure 8.8 Secondary electron images showing parts of agglomerates/aggregates. Agglomerate/aggregate (a) consist of particles emitted during cutting 1.5 mm steel, while agglomerate/aggregate (b) originate from cutting 3.2 mm black steel.

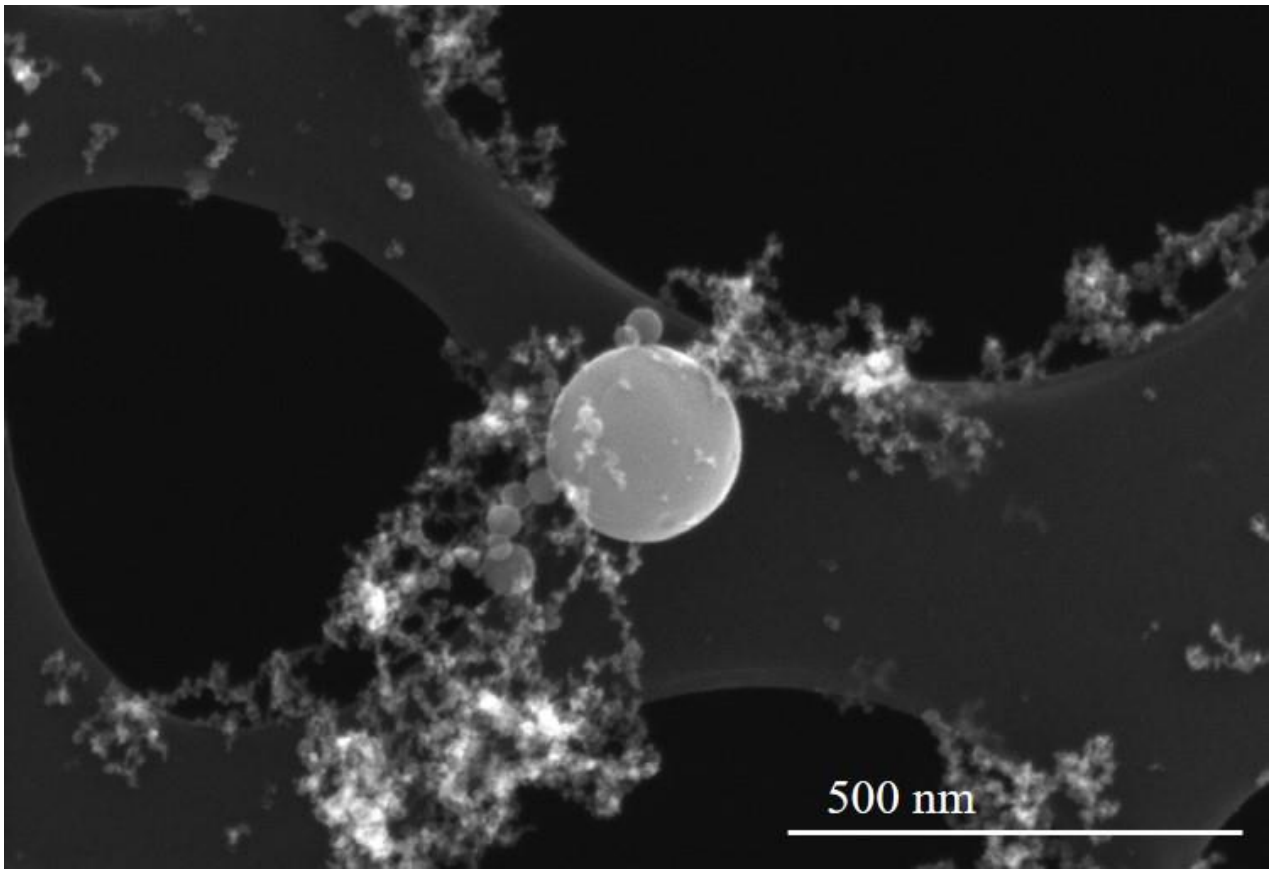

Figure 8.9 Secondary electron image of a large spherical particle (dg > 215 nm) found amongst steel agglomerates/ aggregates with various number of particles.

Particle chemistry by EDX

The elemental composition of selected elements in particles formed during cutting steel, aluminium, and titanium plates were quantified by EDX. The relative atomic percentage (rat %) quantified in more than 10% of the particles analysed is presented in Figure 8.10 and 8.11.

The main element in the particles emitted during cutting steel was Fe. One exception to this was steel with teflon coating, which was cut simultaneously with aluminium 10 mm plates. Low alloy steels, such as black steel and plain steel contained mostly Fe, and either Si or Sn, but also trace amounts of other elements. Elements that were quantified in less than 10% of the particles are defined as trace components, Table 8.2. No trace components were detected in particles from aluminium 0.5 mm.

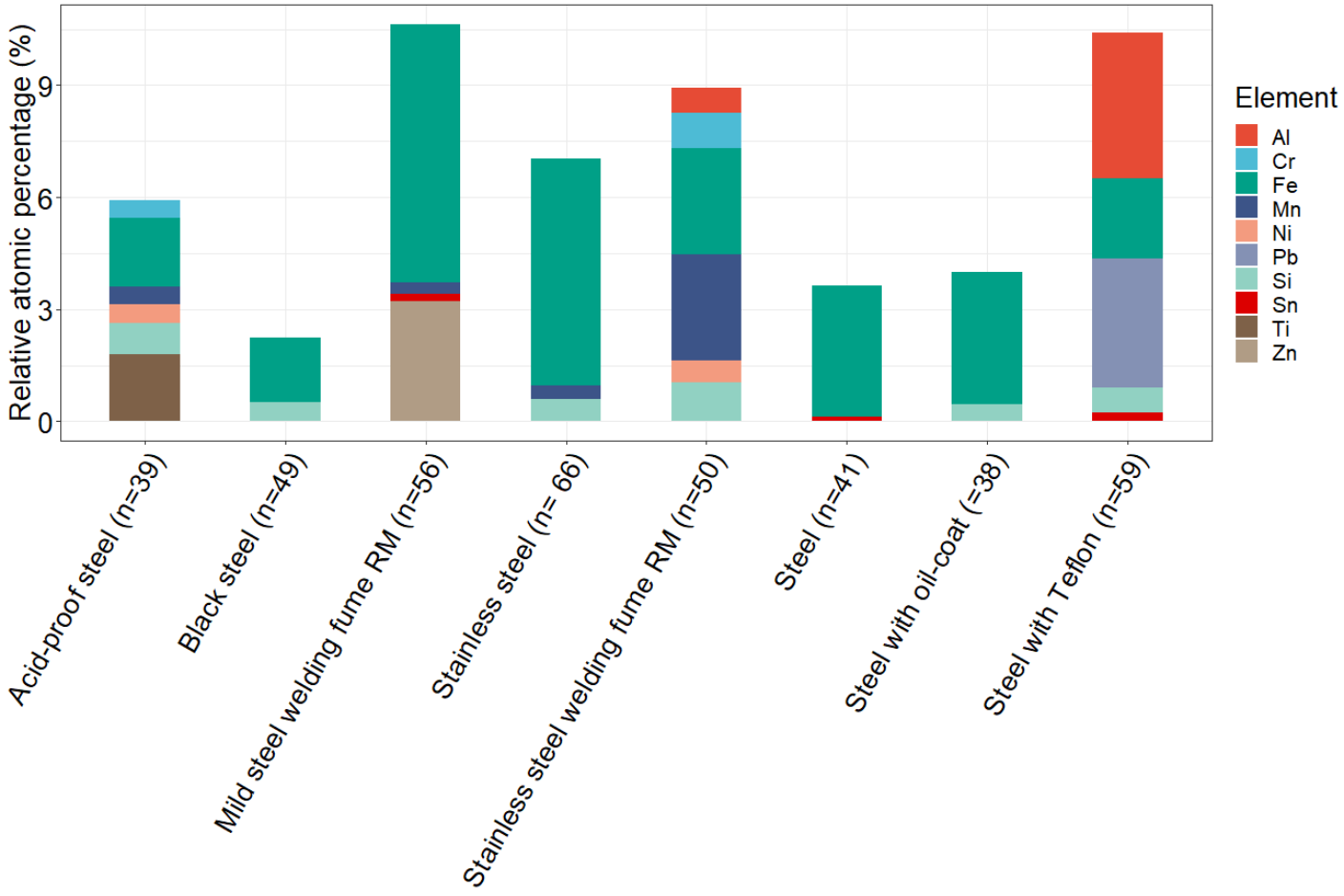

Figure 8.10 Relative atomic percentage of selected elements in particles collected while cutting different steel types measured by SEM-EDX. Note that steel plates with Teflon coating were cut simultaneously with aluminium plates.

Particles from 0.5 mm aluminium plates contained almost 25 rat % of Al in comparison to 10 rat % 10 mm aluminium plates. The 0.5 mm aluminium particles contained ~1 rat % Fe and Mg in total, while 10 mm aluminium contained up to seven different elements with an accumulated atomic percentage of ~7 rat %, see Figure 13. The number of trace components was also different with no trace components versus Cl, Cr, and arsenic (As) in 0.5 mm and 10 mm respectively. The was no difference in the elements found between the different sized primary particles from cutting the same aluminium-based plates.

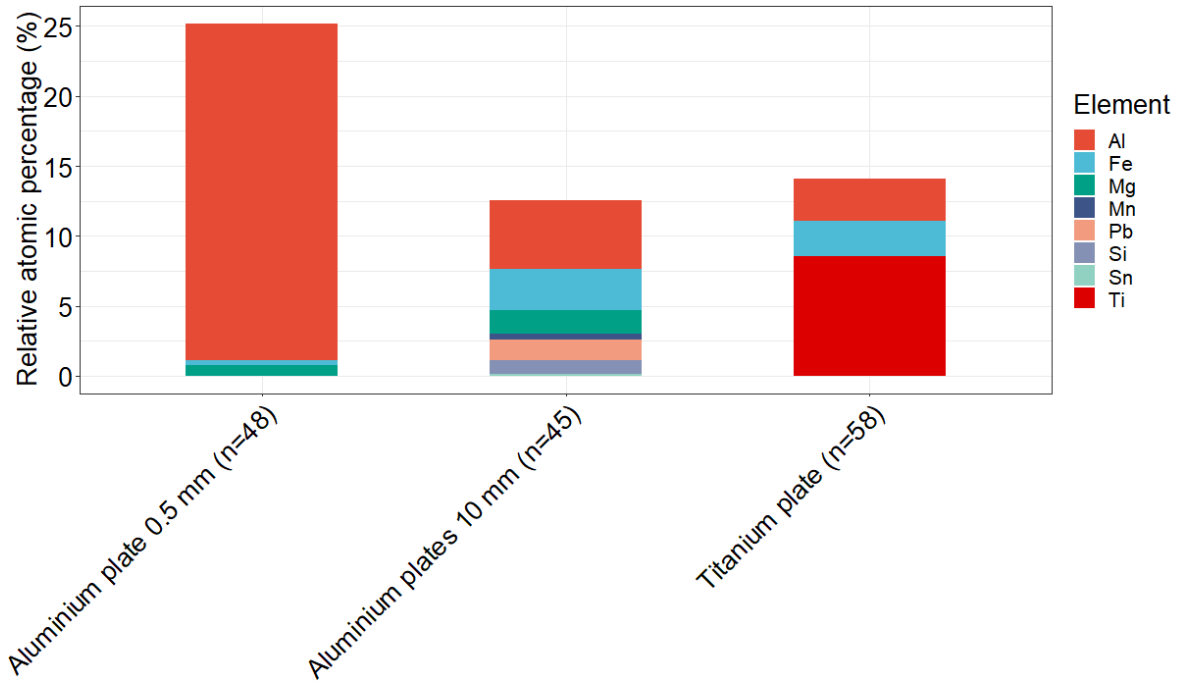

Figure 8.11 Relative atomic percentage of selected elements in particles collected while cutting aluminium-based and titanium-based plates by SEM-EDX.

Table 8.2 Elements quantified in less than 10% of the particles analysed using SEM-EDX

Plate material	Elements
Acid-proof steel (n=30)	Al, Mg, Mo, S, and Sn
Aluminium plates 10 mm (n=45)	Cl, Cr, and As
Black steel (n=49)	Al, Au, Bi, bromine (Br), Hg, antimony (Sb), Sn, and platinum (Pt)
Mild steel welding fume RM (n=56)	Al and Si
Stainless steel (n= 66)	Al and Sn
Steel 3 mm (n=41)	Mn and Si
Steel with oil-coat (=31)	Al, Mg, Ni, and Sn
Steel with Teflon (n=59)	Mg
Titanium plate (n=58)	Mg, Si, S, and calcium (Ca)

Particles with a low Fe content were found amongst steel agglomerates collected during laser cutting acid-proof steel plates. Energy-dispersive x-rays was used to map the elemental composition of the agglomerates/aggregates consisting of primary particles (>50 nm) in Figure 8.12 and 8.13. The agglomerate/aggregate, in the right of Figure 8.12, was Al rich, while the single spherical particle, shown in the right of Figure 8.13 was Ti rich. The bigger agglomerates/aggregates consisting of primary particles (d_g <25 nm) was Fe rich, as seen in the lower right of Figure 8.12 and 8.13.

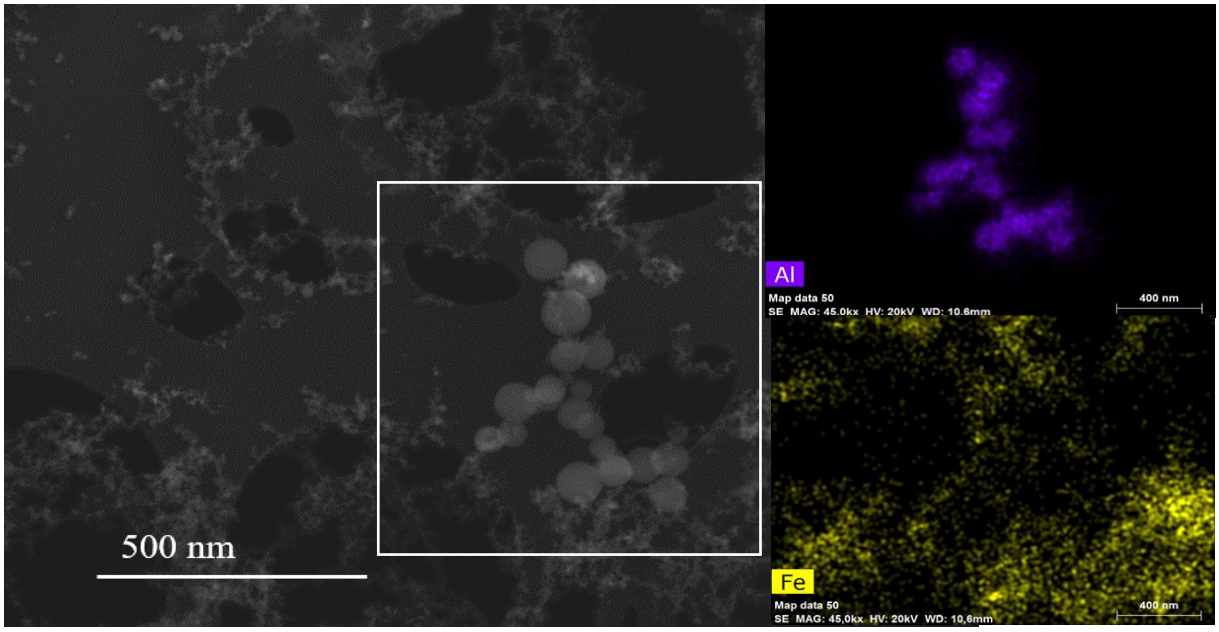

Figure 8.13 Secondary electron image of two different size fractions of primary particles collected from laser cutting acid-proof steel. Mapping by SEM-EDX show that the agglomerates/aggregate with larger primary particles was aluminium-rich while surrounding agglomerates/aggregates were iron-rich.

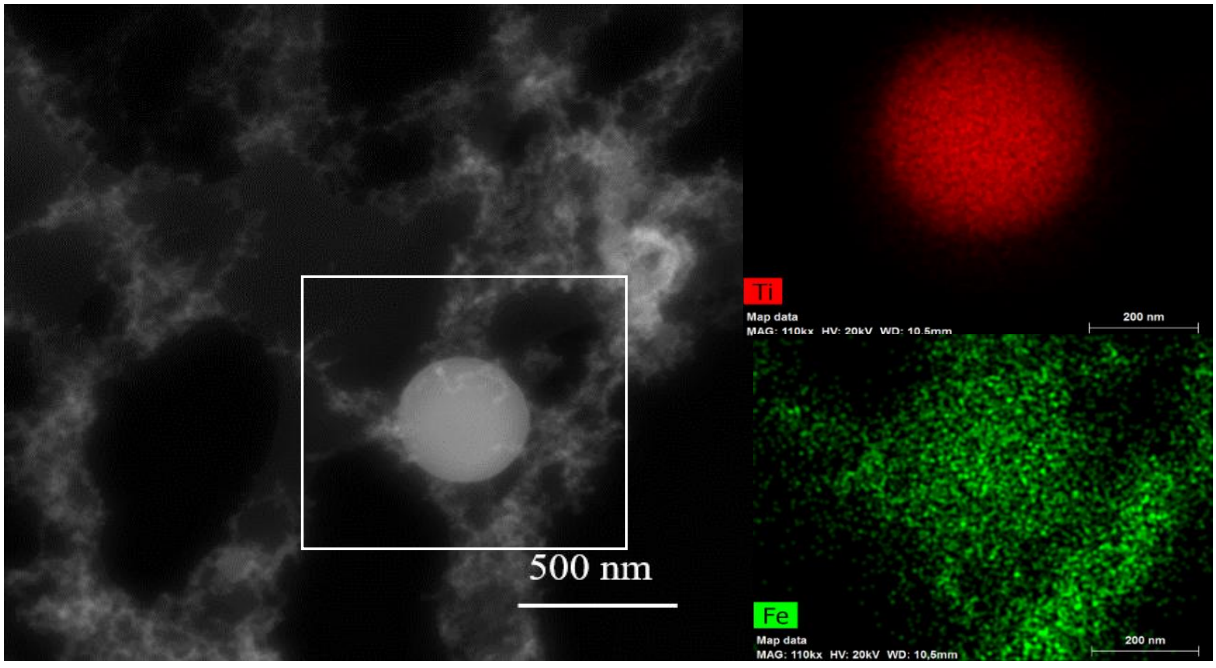

Figure 8.12 Secondary electron image of particles collected from laser cutting acid-proof steel. Mapping by SEM-EDX show that the spherical particle (dg~400 nm) was titanium-rich while the agglomerates/aggregates surrounding it were iron-rich.

Mineral phase determination by EBSD

An EBSD detector was used to determine the mineral composition of particles emitted during cutting of 1.5 mm steel, steel with Teflon coating, the two aluminium-based plate types and the titanium-based plate. Potential phases were suggested prior to phase determination based on the elemental composition determined by EDX, see Figure 12 and 13.

The dominant phase in the steel samples was magnetite (Fe_3O_4). The patterns obtained from particles originating from cutting steel with teflon were blurred, but possible to index. This distortion of the patterns may be due to the coating.

Two different phases were determined in the titanium-based particles, TiO_2 and Ti_2O_3, see Figure 8.14a and b. The dominant phase was found to be TiO_2.

The particles emitted during cutting the 0.5 mm aluminium-based plate contained mainly aluminium (24 rat %) and patterns from these particles were not possible to index. The particles originating from cutting 10 mm aluminium-based plate had 4.9 rat % Al and substantial amounts of Fe (2.9 rat %) and Mg (1.7 rat %). The patterns achieved indicate either iron-silicone-oxide or iron-aluminium-oxide, the latter is most likely due to higher relative amounts of Fe than Si. The highest confidence index was for a spinel type of mineral where Al, Fe, Mg, and Si are combined with oxygen in a cubic crystal system.

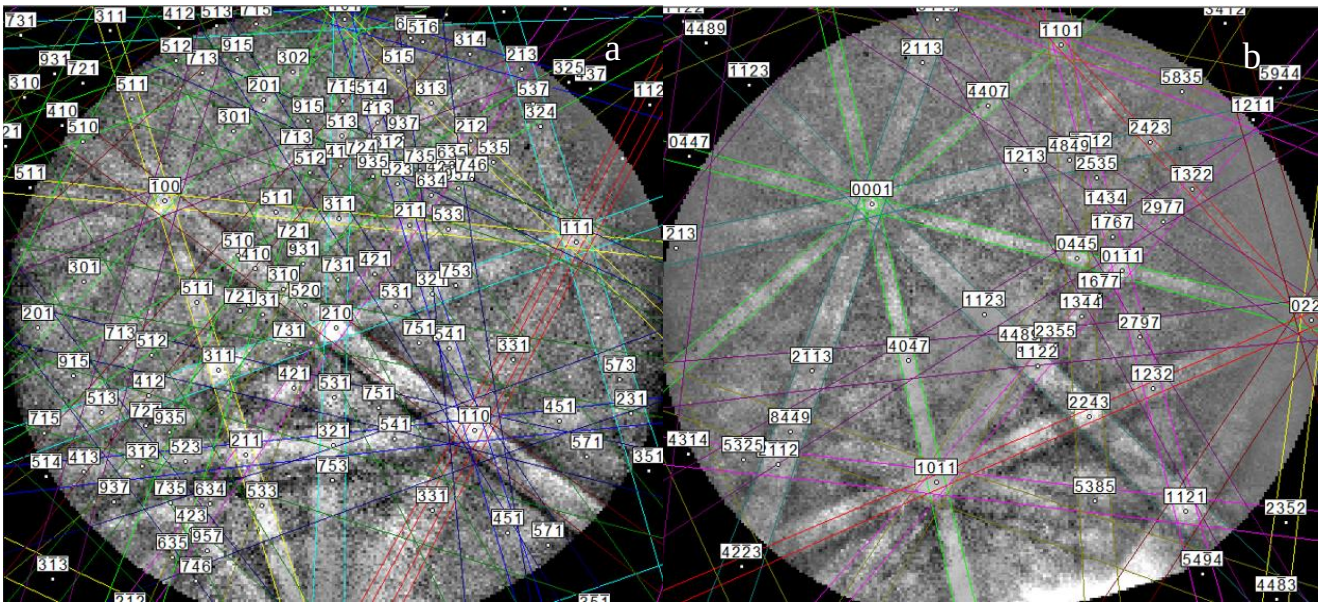

Figure 8.14 Examples of patterns obtained by EBSD and the software-based indexing of these patterns, a) TiO_2 and b) Ti_2O_3 respectively.

Chemical characterization of PM

Particulate matter from laser cutting of selected materials were analysed by ICP-MS and selected elements are presented in Table S2.1 in supplement. The greatest differences between the materials are seen in the main components, Fe and Al. Particles originating from cutting steel plates contained between 0.48 g/g Fe (stainless steel) to 0.64 g/g Fe (steel with oil coating), while PM from cutting aluminium-based plates had 0.14 g/g Fe. Particles emitted during cutting aluminium-based plates contained 0.15 g/g Al, while PM from steel with the highest Al content contained 0.016 g/g Al.

Particles from cutting black and stainless steels contained more Cr than the pure steel plates, 1.8-.2.7 mg/g compared to 0.26-0.39 mg/g, respectively. The Cu concentration was different in PM from cutting the 10 mm aluminium-based plate (76 mg/g) compared to the mean of different steels (1.9 mg/g). The content of Mg, Sn, and Pb were also higher in PM from cutting aluminium-based plate. Manganese, Mo, Ni, S, and Ti variated independently of material type. Zink was only found in PM from the Al-based plates. Low concentrations (µg/g range) of Ag, Cd, Cs, Hg, Li, Sn, V, and W were found in all samples.

The most common alloying metals in stainless steel are Cr, Mn, and Ni. A tertiary diagram with the relative percentage of these elements in relation to each other are shown in Figure 8.15. Also, the certified reference materials are presented in the ternary diagram. Stainless- and black steel-based PM are clustered in the same area as the stainless steel welding fume CRM, while the steel samples (1.5 mm with oil and 3 mm) were clustered closer to the mild steel welding fume CRM. The Cr, Mn, and Ni ratio of PM from cutting the aluminium-based plates were similar to the stainless steel CRM, but the Fe content is lower than the steel samples.

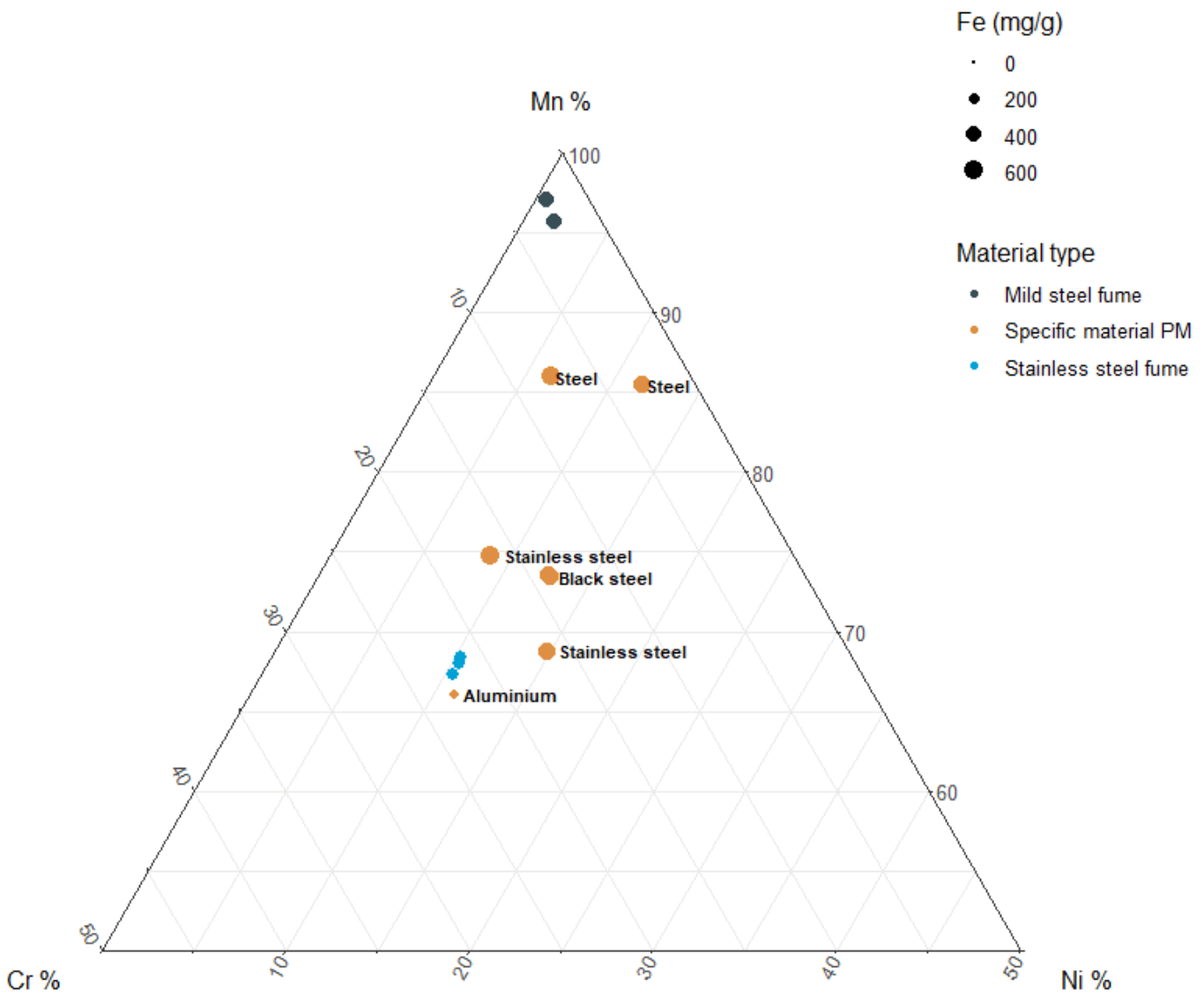

Figure 8.15 The relationship between Mn, Cr, and Ni in PM from cutting specific steel plates, aluminium-based plate, and certified reference material (mild steel fume (MSWF) and stainless steel fume (SSWF)).

Particulate matter were collected from the ventilation systems at two different production sites, 1 and 2 ($PM_{ventilation}$), where the results from site two are based on an average of three samples. The Fe concentration in these samples were comparable, 0.68 g/g and 0.61 g/g, respectively. The main alloying elements, Al, Cr, Cu, Mg, Mn, Ni, and Zn, in the $PM_{ventilation}$ samples are compared in Figure 8.16. Elements with a concentration in the µg/g range are not presented (Ag, Cd, Cs, Hg, Li, Mo, Pb, S, Sn, Ti, V, and W). These elements vary little between the two production sites, see Table S3.1 in Supplements 3.

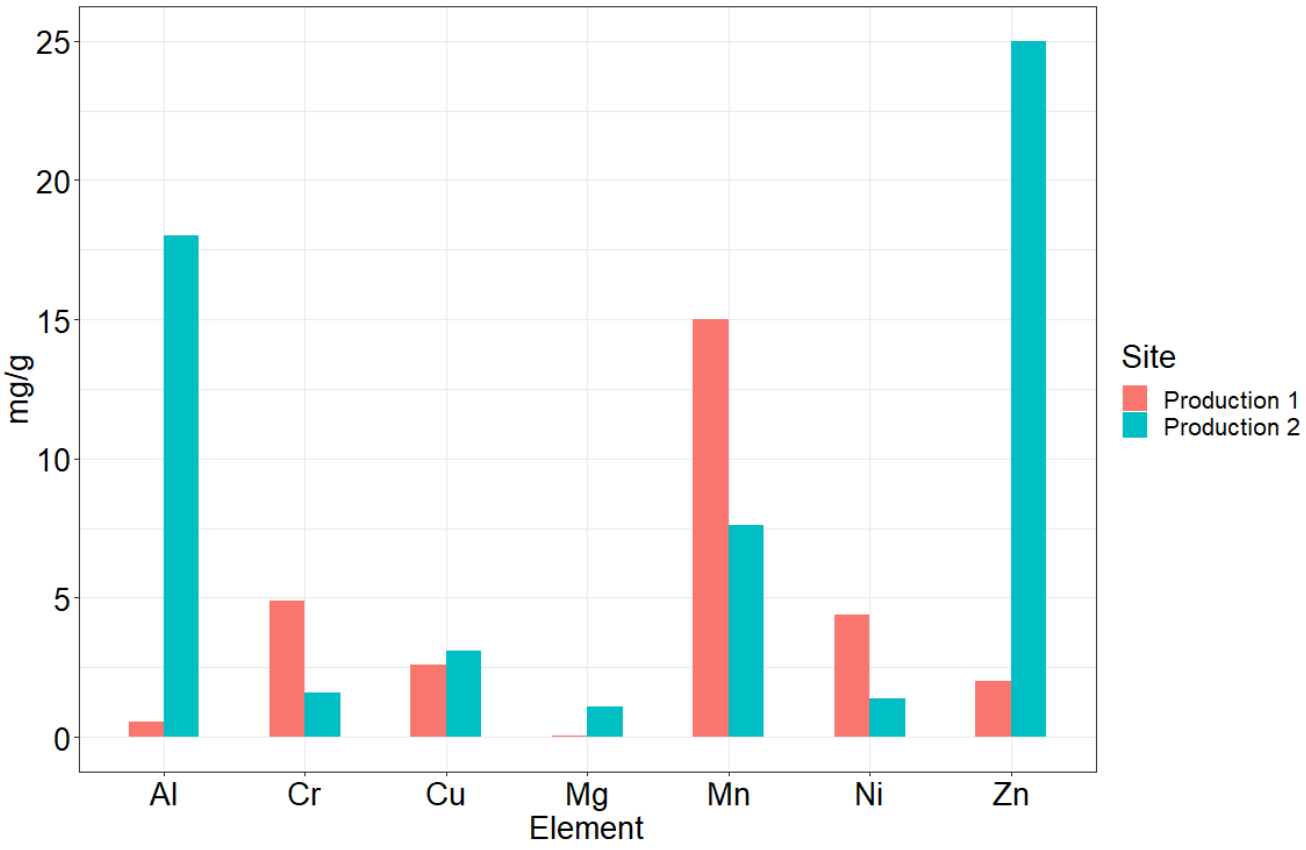

Figure 8.16 Mass concentration of selected elements found in ventilation samples from two different production sites. Values from the Site 2 are based on an average of three samples.

Chapter 9 Discussion

Exposure assessment

All measured respirable dust concentrations of selected metals were below the 20% of OEL's, set by ATIL, for initial exposure assessment with a five sample SEG. The maximum measured concentrations were from different production sites with Ti being from one, Al, Mg, and Zn from another, and lastly Cu, Fe, Mn, Pb and Sn from the last production site. The first two sites had enclosed laser cutters, while the last site had two open laser cutters that were used simultaneously. The five maximum metal concentrations for Cu, Fe, Mn, Pb, and Sn, were from one site with a cutting duration of 265 min. The concentrations in the SEG are as mentioned normalized for an 8-hours shift (480 min), which assumes that the workers are not exposed for the remaining 215 minutes. The exposure to Cu and Pb would be above the 20% of OEL's limit set by initial exposure assessment, if the workers were to be exposed to the same concentrations for the remainder of the shift. Lead is considered in particular due to the toxicity and was found in particles from both materials cut at the site, 10 mm aluminium-based plates and steel with teflon plates, although higher relative atomic percentage in steel with teflon, see Figure 8.10 and 8.11 (Graeme & Pollack, 1998; Yassi et al., 2001). The total chemistry of PM from the 10 mm aluminium-based plates showed that particles from these plates contained almost 400 times higher concentrations of Pb than PM from steel material cut at the other sites, see supplements 3, Table S3.2. The sample from site 3 had the lowest Al concentrations both in mg/m^3 and mg/g total respirable dust, but the difference in plate chemistry explains the higher concentrations of Cu and Pb. The respirable dust sample from the open laser cutters had the greatest total mass of all respirable samples, see Table S3.2 in Supplements 3, despite being based of a 265-minute sampling. This, together with the measured particle concentrations by SMPS outside of the open laser-cutters show that the exposure to particles is greater when working with open laser-cutters. An exposure assessment with a SEG for this particular site or sites with open laser-cutters could be done to determine if workplace exposure is acceptable when working with open-laser cutters.

There was great variation in exposure between workers, Cu, Pb and Sn had the median values being 1000 times lower than the highest measured concentration. Aluminium and Fe showed the least amount of variation of the nine elements presented in Table 8.1. The variation is due to difference in materials cut at the different production sites. For instance, titanium-based plates were only knowingly cut at one site and higher concentrations of Ti at this site are therefore expected. Steel materials were cut at all sites, which result in low variation of Fe. The

grouping of elements in the respirable dust can be explained by different alloying elements being common in different materials. Manganese is commonly used in steel, while Mg and Zn are common alloying metals in aluminium alloys (Callister & Rethwisch, 2020). The relation between elements in plate material and PM can be an important part of the workplace characterization in a workplace exposure assessment. The production site with the highest Al content in respirable dust samples did not cut aluminium-based plates by laser-cutter on the day of the sampling. The specific material samples from the steel cut at this had between 2.1 mg/g and 22 mg/g Al accounting for some of the Al. However, the exposure in the workplace is not dependent on one single process, but multiple and Al from other processes than laser-cutting cannot be ruled out. All work conducted in a workspace will affect the exposure.

An earlier study by Berlinger et. al (2019a) showed high short-term air concentrations of Cr, Fe, Mn, Ni and Cu in PM in workplaces with hot work processes. However, the measured maximum concentrations in this study were below the OELs. The particle number concentrations were higher within the laser-cutters than outside, as supported by the SMPS data. Workers conducting maintenance inside the laser chamber could be exposed suspend dust remaining inside the instrument after cutting, leading to possible high short-term exposure. Short-term exposure tests, duration up to 15 min at peak concentrations, can be made if the short-term exposure is suspected to be high. The short-term exposure can be 100% to 200% the OEL's in Table 7.2, dependent on if they are $1 \leq 100$ or ≥ 1 mg/m^3 (Arbeidstilsynet, 2021a). Elements in question for short term exposure would be Fe due to the general high Fe concentrations in steel fume, in addition to Al, Cu, Cr, Mn, Pb, and Zn.

Particles collected from the ventilation system of production sites one and two show a similar grouping of elements as will be disused further. It seems to be a connection between the amount of Mn/Cr/Ni and Al/Zn in the $PM_{ventilation}$ indicating that these groups are from specific material types. Manganese, Cr, and Ni are normally found in stainless steel and Mg is a common additive in Al-alloys. The amounts of Zn found in specific material PM from aluminium-based plates are a tenfold lower than the Al concentrations. The Zn content was higher than the Al in the ventilation samples from both sites. Only one sample was made for specific material analysis of aluminium-based plates, but these plates were not cut at the same sites as the $PM_{ventilation}$. The difference between $PM_{ventilation}$ and the specific PM from Al-material can be explained by cutting other Al-based plates at another time. A ternary diagram was made to further explore the relationship between Cr, Mn and Ni in specific materials and compare these with certified reference materials, see Figure 8.15. There was a difference between the stainless- and black-

steel PM and the mild steel PM although the mass percentage of Cr, Mn, and Ni were small. The mild steels had around 85% Mn and 5-15% Cr and Ni, relative to each other and clustered in the uppermost corner together with mild steel CRM. The black- and stainless steel samples had relatively 70-75% Mn, 10-15% Cr, and ~15% Ni. These samples clustered around the stainless steel CRM. Stainless steel contains generally higher weight percentages of alloying metals explaining the difference in relative percentage. The aluminium sample had the most similar Cr/Mn/Ni ratio, but the Fe content is almost 400 mg/g higher in the steel samples. The results show that the ratios between different elements can be used, in addition to main component, to identify the sources of the particles, which is useful in exposure assessments.

The high variation between the samples within the defined SEG raises the question of whether the assumption of similar exposure in the SEG can be accepted. The SEG includes three different production sites, with five workers on three different production sites. Two and two of the values are dependent on each other as they are collected from same shift. The combination of open and enclosed laser-cutters makes the different sites less comparable. Further exposure assessments including more production sites and different shifts at each site may provide a better indication of the overall exposure within the industry. The low number and dependency of samples on one another make these samples unsuitable for e.g. PCA analysis (Jolliffe, 2002). Furthermore, one or more samples out of five were below the LOD for multiple elements, Zn, Sn and Cd raising the question of how to treat nondetect values without jeopardizing the quality of the results of a PCA analysis (Helsel, 2005; Helsel, 2006).

Size distribution dominated by particles < 500 nm

Nearly all the particles measured in the work atmosphere by APS, had a d_{ae} below 2 µm, with a peak at 0.9 µm, meaning that all the airborne particles are within the respirable fraction, see Figure 2.1. The mean peak concentrations in the work atmosphere were 112 particles/cm^3, see Figure 8.1. The airborne particle concentrations show a similar size distribution as Pena (1998), but at lower concentrations as the APS data was measured outside of the laser-cutters. Occupational exposure limits from ATIL are often dependent on the particle type in addition to air mass concentration, see Table 7.2, of OEL's in subchapter method of exposure assessment. This is the case for Al, Pb, Mn, and Cu to mention some, e.g., Cu has an OEL for smoke 0.1 mg/m^3 while the corresponding limit for dust is 1 mg/m^3. This is due to a different size distribution of the particle types and hence penetration in the respiratory system. A smaller particle size also results in a greater surface area and a higher number of particles per mass unit. Manganese e.g., has different OEL's for the inhalable and respirable fraction.

The SMPS data from the open laser cutters, see Figure. 8.2 in results, provide an indication of the work atmosphere concentrations of particles <500 nm. These data show a main mobility diameter below 100 nm at considerably higher concentrations, 10^4 times higher than the particles measures by APS. This indicates that a substantial number of particles with a d_{mob} below 100 nm could be present in the work atmosphere for these workers. The workplace exposure in terms of number of particles are thereby greater in the fraction <500 nm d_{mob} than in the size range measured by APS. Moreover, the concentrations of particles in Figure 8.2, are increasing with decreasing particle diameter (d_{mob}) and multiple laser-cutters operated simultaneously. The SMPS inlet was placed outside of an enclosed laser cutter in the pilot study conducted during spring of 2019. It showed a similar size distribution (10 – 200 nm d_{mob}), but a lower peak normalised particle concentrations at 20 000 particles/cm^3 (Hammer, 2019). The difference in peak normalized particle concentrations between open and enclosed laser cutters, measured in the work atmosphere further support a greater exposure to PM in open laser cutter environments. In terms of the assumption by ATIL (2021b) that the potential health risk from laser-cutting is like the one of welding, is the dominant range particle size distribution of different welding fumes, with respect to mass, between 0.1 to 1 µm (Berlinger et al., 2011; Isaxon et al., 2009). The particle exposure in the case open laser cutters however seems to have a somewhat lower particle distribution. Regardless, are most of the particles from both welding and laser-cutting in the respirable fraction, see Figure 2.1.

The peak particle size concentrations measured inside the laser chamber seemed to differ based on the type of material. The peak particle number concentrations also seem to increase with decreasing plate thicknesses, regardless of the type of steel. Black steel and steel with a thickness of 3 mm both had peak number concentrations around 100 nm d_{mob}, with 1.5 mm steel having a peak at 146 nm d_{mob} and 78 nm d_{mob} for 3 mm acid-proof steel. There was no clear sign of increasing peak particle size concentration with decreasing plate thickness for the three stainless steels cut by fiber-laser. The difference may thereby be because of different materials and/or type of laser used. The size distribution measured by SMPS of particles from aluminium-based plates had a size from 55 to 615 nm d_{mob}, with two peak number concentrations, at 95 nm and 235 nm d_{mob}. The particles observed in SEM show agglomerates from two different fractions of primary particles. The smallest fraction ~10 nm d_g complements earlier findings of primary particles (Noskov et al., 2020; Ullmann et al., 2002). The double peak size distribution indicates that the larger primary particles (>100 nm) viewed in SEM appear as agglomerates/aggregates due to stacking on the TEM filter, but are measured individually by

SMPS. The smaller primary particles are found as agglomerates/aggregates in SEM causing both a higher dg and d_{mob} by SMPS. The overall particle size distribution within the laser chamber is similar to earlier findings of laser-based manufacturing (Dazon et al., 2020; Elihn & Berg, 2009; Elihn et al., 2011).

The observed normalized particle concentrations increase as the plate thicknesses decreases, see Figure 8.5, with the same size distribution. These findings fit with earlier studies conducted by Pena et al. (1998). The increase in particle number concentration can be explained by the fact that the material is being exposed to the same amount of energy from the laser beam in all cases. A thinner plate will have a lower area for energy absorption causing the material to vaporize at a higher rate. This may lead to the greater production of aerosols. A thicker plate, however, will have a greater area for energy absorption, and the material surrounding the laser beam could melt rather than vaporize.

The impression from SEM images of particles from titanium-based plates was that the d_g of primary particles was ~50 nm or less. Larger spherical particles (>400 nm d_g) that occurred sporadically, see Figure 8.3b, are not seen directly in the SMPS size distribution curve, as the y-axis of are logarithmic with concentrations in x 10^6. The observed size distribution from 50 to 350 nm d_{mob} can be explained by agglomeration/aggregation of primary particles as observed in steel and aluminium and steel particles. The agglomerates/aggregates are not individually distinguishable in SEM due to stacking of particles, but earlier data indicates that titanium fume particles agglomerate/aggregate similarly to steel (Cyr et al., 2000). The size distribution observed by SMPS and SEM secondary electron images supports that the particles agglomerates/aggregates as the sizes are greater than the primary particles themselves.

One important note for two of the samples in the SMPS data for aluminium- and titanium-based plates are based on two measurement cycles due to short cutting time. Agglomeration and/or aggregation happen within milliseconds of the laser vaporizing the metal (Ullmann et al., 2002). The distance from the cutting surface to the SMPS inlet may therefore affect the size distribution viewed. The difference in size distribution when running two consecutive SMPS cycles of one minute and 20 seconds were hence compared with an overall mean of 91 cycles, Supplements 4. A difference in size distribution was observed between the 6 tests, consisting of 2 random consecutive cycles, and the mean value over 91 cycles. The size distributions had either a similar main peak, or a main concentration peak at a lower d_{mob}. These variations might be due to the distance from the laser-beam to the inlet to the SMPS affecting the size distribution as a longer distance will allow for longer “travel time” to the inlet and thereby more

agglomeration/aggregation. Fewer measured cycles will thereby not make up for possible differences in distance from the SMPS inlet. However, it must also be taken in consideration that the overall mean will be affected by changing the plates as they were cut.

A fourfold increase in airborne particle concentrations were observed when cutting both aluminium-based plates and steel with teflon plates simultaneously. An increase is to be expected when two laser-cutters are in use, but the size distribution curve for the double cutting seem to be steeper towards the lower particle diameters. The particle distribution for aluminium-based plates alone however flattens out below 65 nm d_{mob}. The steeper particle size distribution curve may be because of the teflon coating on the steel plates. Teflon will vaporize before steel as it has a lower melting point, 327 C° than both steel (1230°C-1565°C) and aluminium (500°C - 660°C) (ASM-International, 2002; Callister & Rethwisch, 2020). The plates were only coated with teflon on one side which was facing away from the laser, but the evaporation may still be seen in the SMPS data.

Morphology

Common for particles from all different materials collected from laser-cutting were spherical primary particles in chain like agglomerates/aggregates. This is comparable to morphology determined in earlier studies of laser manufacturing and other hot work processes (Antonini et al., 2006a; Noskov et al., 2020; Ullmann et al., 2002; Zeidler-Erdely et al., 2012). The similarities are expected as these types of particles are formed through condensation of metal vapor (Walter et al., 2013). The observed SMPS data confirms this through a higher d_{mob} than what a single particle would correspond to and agglomeration/aggregation must have taken place.

Whether a particle is an agglomerate held together by weak forces or an agglomerate of strongly bound primary particles cannot be determined by SEM analysis. The degree of agglomeration/aggregation seem to differ from visible primary particles to not distinguishable particles, see Figure 8.7a and 8.7b. Primary particles down to a diameter of ~10 nm d_g were still distinguishable within the agglomerate/aggregate in Figure. 8.7a. A solution for determination of agglomeration vs aggregation is to use transmission electron microscopy (TEM), a technique where the electrons transmitted through the particles are used to form an image. Transmission images would potentially give information on both how the agglomerate/aggregates are bound together and a difference in chemical composition within particles (Goldstein et al., 2018; Noskov et al., 2020). An agglomerate with loosely bound primary particles may possibly break

apart when entering the respiratory system, causing a lower diameter. Agglomerates may have a greater surface area than aggregates, if the agglomerate separate into primary particles in the lungs. An increased surface area may also increase the overall solubility of the particle.

Relationship between exposure and characterisation of metal fume from cutting different metal-containing plates

Particle chemistry by EDX was done comparing several particles, giving an overview of the chemical composition. A difference in the number of elements found, or the elemental complexity, was observed in particles from steel plates. Overall, Fe was the element with the highest relative concentrations in steel material. Simple steel alloys such as black steel and plain steel contained detectable amounts of Fe, Sn, and Si, apart from the background concentrations of C, O, and Cu from the TEM grid and vaporization of the sample in the chamber. Trace amounts of other elements were quantified in less than 10% of the analysed particles giving an indication of the purity of the plate material. Black steel, a low alloy steel, had trace amounts of multiple elements (e.g., Sn, Bi, Br, and Al) which were not detected in steel with and without oil coating. The particles from 0.5 mm Al-based plate have an Al content of almost 25 rat % in comparison to the 10 mm plate with only 10 rat %. The difference between the Al particles is likely due to the intended use of the plates. A relative pure Al-plate is needed to be rolled into thin sheets (Callister & Rethwisch, 2020), while a thicker plate will have higher concentrations of alloying elements to achieve specific properties. A sample for ICP-MS was not collected from 0.5 mm Al due to low cutting time and the total chemistry and can thereby not be discussed.

Certified reference materials for ICP-MS were analysed by SEM-EDX for comparison with particle chemistry. The elements detected in stainless steel welding fume were similar to the particle chemistry of fume particles from acid-proof steel, with exception of Ti which will be discussed in a later paragraph. The particles from stainless steel, however, were not similar to the stainless steel welding fume certified material other than the presence of Mn. Both Cr and Ni were quantified when viewing the ICP-MS data, but at lower concentrations than Mn. Chromium and Ni were not visible by SEM-EDX as the relative amounts in the particles were too low. The possibility of identifying particles from low and high alloy steels interesting due to the known toxicity of alloying elements such as Cr, Mn, and Ni (McCarrick et al., 2019; McNeilly et al., 2004; Shoeb et al., 2017). High alloy steels usually have higher concentrations of Cr, Mn and Ni and these would thereby be helpful to identify in metal fume sample of unknown origin. Determination of particles from low alloy steels will be more difficult as the

relative amounts of each alloy are lower. A solution may be to use a longer acquisition time for each particle scan to increase the analyte signal.

It is possible to distinguish between particles of different origins by the use of SEM-EDX. Particles of different origins were found within acid-proof steel particles, see Figure 8.12 and 8.13. The particle morphology for all different materials was similar with spherical particles in chainlike agglomerates/aggregates, making it impossible to differ between particles based on morphology. Particles with different chemistry were found in one of the acidproof steel samples, indicating that there can be particles originating from the cutting previous materials. These particles seemed to have a greater d_g of primary particles than the acid-proof steel particles. A greater size may indicate a longer residence time and might even be secondary particles caused by agglomerates growing into a greater spherical particle with increased time and temperature (Eggersdorfer & Pratsinis, 2014; Ullmann et al., 2002). The chemistry of steel with teflon particles by SEM-EDX are more difficult to compare with the known alloying metals in steel, as the relative amounts of both Al (3.9 rat %) and Pb (3.5 rat %) were higher than the amount of Fe (1.1 rat %). The overall composition is similar to the particles from 10 mm Aluminium-based plates cut simultaneously.

Mineral phase determination by EBSD confirmed that predominant mineral phases are oxides of the alloying elements. The dominant phase in steel particles, collected from 1.5 mm steel plate and steel with teflon, was magnetite. This was further confirmed by XRD of filter collected stainless steel and mild steel particles, but alpha-Fe was additionally determined in stainless steel fume particles (Ervik, 2021). Particles (>30 nm) from laser additive manufacturing have been shown to have a metal core and an oxidized outer layer. The XRD results from this work indicate that this might also apply for laser cutting, which is a similar process. The metal core was not detectable by EBSD as the electron beam may not penetrate the core of these particles. The major components in titanium particles were determined to be Ti, Fe, and Al, with the primary phase being titanium oxides. The complex chemistry of the particles from 10 mm Aluminium-based plates was reflected in the mineral phase as spinel oxides. Elements which form di- or trivalent cations can condense into a spinel structure. The probability of spinel groups increases with an increased weight percent of alloying metals in the material. The 10 mm Aluminium PM contained 15 weight percent Al and 14 weight percent Fe according to total element analysis. The total chemistry supports the determined spinel structure found through EBSD analysis. Stainless steel could possibly also create a spinel structure due to alloys like Cr and Mn, but contain ~50% Fe or more according to the total

element analysis. This chemical composition may be iron oxides determined by EBSD in the mild steel sample.

The OEL's for specific elements are not only dependent on the particle origin, but also chemistry in terms of mineral phase. Elements such as Fe, Cr, Mg, and Ti are specifically mentioned as oxides in the OEL's, Table 7.2 in Method and Materials. The solubility and thereby the toxicity of the particles are dependent on the chemical properties, as the mineral phase. The information of total chemistry, mineral phase and particle size would be important information if the toxicity of metal fume particles from laser- cutting were to be tested.

The technique of mineral phase determination by EBSD is most used for flat and polished geological samples, as a sufficiently large mineral crystal form is needed to achieve a signal. It was challenging to achieve patterns by EBSD on the metal fume particles because of the low size of primary particles. The particle must have a large enough size to have a crystal structure and the right placement in relation to the detector. It seemed to be a lower cut off for reviving EBSD patterns from primary particles < 100 nm to identify of the mineral phases present, but this needs to be further investigated. Determination of physiochemical properties of individual particles in workplace aerosols by EBSD has a great potential. Nevertheless, for an overall mineral phase determination of a sample would a bulk analysis by XRD be a good option.

Chapter 10 Conclusion

The workplace exposure to PM in the Norwegian laser cutting industry, as well as the physical and chemical properties of the particles, were investigated in this study.

The maximum respirable PM concentrations (mg/m^3) in the SEG were below the 20% of the OEL's limit set by a five-sample initial test. A variation of up to 1000 times difference between the median and maximum metal concentrations was noticed. The least amount of variation was found in main alloying elements such as Fe and Al, while the variation was greatest in Cu, Pb, Zn, and Sn. A dependency was found between the materials cut at the site and the metal concentrations in respirable dust. A grouping of elements Al, Mg, and Zn, and Cu, Fe, Mn, Pb, and Sn was found in the $PM_{ventilation}$ samples and respirable dust, and was dependent on the materials cut on the site. The total mass of the respirable dust from the site with open laser cutters was higher than the enclosed laser-cutter sites and shows a higher exposure to PM in workplaces with open laser-cutters. Thus, a new initial exposure assessment is recommended for sites with open-laser cutters to achieve a more complete image of the overall exposure in the industry. A dependency between respirable dust samples prevented further statistical analysis of the data material.

The common denominator for particle morphology were spherical primary particles in chain like agglomerates/aggregates, as was expected from metal fume. Primary particles with a d_g down to a diameter of ~10 nm were observed by SEM, but primary particles with smaller diameter cannot be excluded. The size distribution of particles measured inside of the laser-chamber showed a general size distribution from 30 to 350 nm d_{mob} with different peak concentrations due to different types of lasers, material, and plate thickness. The normalized particle concentrations increased with decreasing plate thickness. The size distribution measured in the work atmosphere revealed that most particles had a d_{mob} below 300 nm, and thereby being in the respirable fraction.

The chemical properties of the material cut were reflected in the determined particle chemistry, with both SEM-EDX analysis and total chemistry by ICP-MS measuring highest concentrations of main alloying metals. Specific material PM samples showed that the Fe content alongside Cr/Mn/Ni ratio can be used to differentiate between low and high alloy steels. Fixed ratios alongside the grouping of elements observed in respirable dust can be used to identify particle sources and be a helpful tool in exposure assessments. The determined mineral phases by EBSD in combination with EDX were oxides of the alloying metals, supported by later XRD analysis.

Overall, the combined usage of SEM, ICP-MS, and real-time spectrometry gave a detailed overview of the exposure to particles from laser cutting as well as the physical and chemical properties of the particles.

Chapter 11 Notes to further work

The conducted exposure assessment was affected by the Sars-CoV-2 (COVID 19) and the number of different production sites and days of sample collection was reduced as a consequence of various lockdowns. The result was an initial exposure assessment rather than a detailed assessment, with two and two dependent samples in the SEG. It was however possible to conclude that the overall exposure was acceptable, but the exposure from open laser-cutters seemed to be higher than enclosed laser-cutters. An initial exposure assessment for workers using these machines is recommended to ensure appliance with OEL's.

The use of EBSD in combination with EDX was successfully applied to identify mineral phases of workplace particles. There seems to be great potential in the technique, but more research on the subject and development of standardized methods are needed. Nevertheless, the use of EBSD-EDX should be combined with XRD to provides an overall description of the material phases. The EBSD analysis gives information on single particles, where e.g., morphology may affect the results. A bulk determination of mineral phases, however, is achieved by XRD. Using XRD on collected filter dust, such as the specific material PM from this thesis, is a promising tool for a wide range of occupational settings and should thus be explored further. The use of XRD multicomponent tools for quantification of mineral phases is also an unexplored field when it comes to dust collected on filters.

Transmission electron microscopy could be utilized on the same samples as the SEM. The technique could give detailed information like whether particles consist of agglomerates or aggregates, and confirm the presence of a metallic particle core as seen by XRD.

References

Antonini, J. M. (2003). Health effects of welding. *Critical Reviews in Toxicology*, 33 (1): 61-103. doi: Doi 10.1080/713611032.

Antonini, J. M., Afshari, A. A., Stone, S., Chen, B., Schwegler-Berry, D., Fletcher, W. G., Goldsmith, W. T., Vandestouwe, K. H., McKinney, W., Castranova, V., et al. (2006a). Design, construction, and characterization of a novel robotic welding fume generator and inhalation exposure system for laboratory animals. *Journal of Occupational and Environmental Hygiene*, 3 (4): 194-203. doi: 10.1080/15459620600584352.

Antonini, J. M., Santaimaria, A. B., Jenkins, N. T., Albini, E. & Lucchini, R. (2006b). Fate of manganese associated with the inhalation of welding fumes: Potential neurological effects. *Neurotoxicology*, 27 (3): 304-310. doi: 10.1016/j.neuro.2005.09.001.

Antonini, J. M., Sriram, K., Benkovic, S. A., Roberts, J. R., Stone, S., Chen, B. T., Schwegler-Berry, D., Jefferson, A. M., Billig, B. K., Felton, C. M., et al. (2009). Mild steel welding fume causes manganese accumulation and subtle neuroinflammatory changes but not overt neuronal damage in discrete brain regions of rats after short-term inhalation exposure. *Neurotoxicology*, 30 (6): 915-925. doi: 10.1016/j.neuro.2009.09.006.

Arbeidstilsynet. (2021a). *Grenseverdier for kjemisk eksponering*. Available at: https://www.arbeidstilsynet.no/tema/kjemikalier/grenseverdier-for-kjemisk-pavirking/ (accessed: 12.07).

Arbeidstilsynet. (2021b). *Varmt arbeid*. Available at: https://www.arbeidstilsynet.no/tema/kjemikalier/varmt-arbeid/ (accessed: 05.04).

ASM-International. (2002). *Thermal properties of metals*. Materials Park, OH, USA: ASM International. p. 560.

Bandli, B. R. & Gunter, M. E. (2012). Electron backscatter diffraction from unpolished particulate specimens: Examples of particle identification and application to inhalable mineral particulate identification. *American Mineralogist*, 97 (8-9): 1269-1273. doi: 10.2138/am.2012.4155.

Berlinger, B., Naray, M., Sajo, I. & Zaray, G. (2009). Critical Evaluation of Sequential Leaching Procedures for the Determination of Ni and Mn Species in Welding Fumes. *Annals of Occupational Hygiene*, 53 (4): 333-340.

Berlinger, B., Benker, N., Weinbruch, S., L'Vov, B., Ebert, M., Koch, W., Ellingsen, D. G. & Thomassen, Y. (2011). Physicochemical characterisation of different welding aerosols. *Anal Bioanal Chem*, 399 (5): 1773-80. doi: 10.1007/s00216-010-4185-7.

Berlinger, B., Skogen, U., Meijer, C. & Thomassen, Y. (2019). Workplace exposure to particulate matter, bio-accessible, and non-soluble metal compounds during hot work processes. *Journal of Occupational and Environmental Hygiene*, 16 (6): 378-386. doi: 10.1080/15459624.2019.1594841.

Boss, C. B. & Fredeen, K. J. (1997). *Consepts, Instrumentatin, and Techniques in Inductively Coupled Plamsa Optical Emission Spectrometry*. 2 ed. USA: Perkin-Elmer.

Brandon, D. & Kaplan, W. D. (2008). *Microstructural characterization of materials*. 2 ed. Chichester, West Sussex, England: John Wiley & sons.

Brown, J. S., Gordon, T., Price, O. & Asgharian, B. (2013). Thoracic and respirable particle definitions for human health risk assessment. *Particle and Fibre Toxicology*, 10. doi: Artn 12 10.1186/1743-8977-10-12.

Cabanillas, E. D., Creus, M. F. & Mercader, R. C. (2005). Microscopic spheroidal particles obtained by laser cutting. *Journal of Materials Science*, 40 (2): 519-522. doi: DOI 10.1007/s10853-005-6118-y.

Cai, H., Chaudhary, N., Lee, J., Becker, M. F., Brock, J. R. & Keto, J. W. (1998). Generation of metal nanoparticles by laser ablation of microspheres. *Journal of Aerosol Science*, 29 (5-6): 627-636. doi: Doi 10.1016/S0021-8502(97)00465-5.

Callister, W. D. & Rethwisch, D. G. (2014). *Materials Science and Engineering* 9ed. Hoboken NJ, USA: Johan Wiley & sons.

Callister, W. D. & Rethwisch, D. G. (2020). *Callister's materials science and engineering*. Global edition ed. New York, USA: John Wiley & sons.

Caristan, C. L. (2004). *Laser cutting - Guide for Manufacturing*. Dearborn, Michigan, USA: Scociety of Manufacturing Engineers.

Carvalho, T. C., Peters, J. I. & Williams, R. O. (2011). Influence of particle size on regional lung deposition – What evidence is there? *International Journal of Pharmaceutics*, 406 (1-2): 10.

CEN. (1993). *Workplace atmospheres-size fraction definitions for measurement of airborne particles (Report No. BS EN 481:1993)*. London, England: CEN.

CEN. (2019). *Workplace exposure - Measurement of exposure by inhalation to chemical agents - strategy for testing compliance with occupational exposure limit values*. Brussels, Belgium: CEN.

Cena, L. G., Keane, M. J., Chisholm, W. P., Stone, S., Harper, M. & Chen, B. T. (2014). A Novel Method for Assessing Respiratory Deposition of Welding Fume Nanoparticles. *Journal of Occupational and Environmental Hygiene*, 11 (12): 771-780. doi: 10.1080/15459624.2014.919393.

Cherrie, J. W. & Aitken, R. (1999). Measurement of human exposure to biologically relevant fractions of inhaled aerosols. *Occupational and Environmental Medicine*, 56 (11): 747-752. doi: DOI 10.1136/oem.56.11.747.

Cyr, M., Carles-Gibergues, A. & Tagnit-Hamou, A. (2000). Titanium fume and ilmenite fines characterization for their use in cement-based materials. *Cement and Concrete Research*, 30 (7): 1097-1104. doi: Doi 10.1016/S0008-8846(00)00290-8.

Dazon, C., Porcheron, E., Journeau, C., Suteau, C., Chagnot, C., Doyen, I., Excoffier, E. & Roulet, D. (2020). Characterization of chemical composition and particle size distribution of aerosols released during laser cutting of fuel debris simulants. *Journal of Environmental Chemical Engineering*, 8 (4). doi: ARTN 103872 10.1016/j.jece.2020.103872.

DeCarlo, P. F., Slowik, J. G., Worsnop, D. R., Davidovits, P. & Jimenez, J. L. (2004). Particle morphology and density characterization by combined mobility and aerodynamic diameter measurements. Part 1: Theory. *Aerosol Science and Technology*, 38 (12): 1185-1205. doi: 10.1080/027868290903907.

Eggersdorfer, M. L. & Pratsinis, S. E. (2014). Agglomerates and aggregates of nanoparticles made in the gas phase. *Advanced Powder Technology*, 25 (1): 71-90.

Elihn, K. & Berg, P. (2009). Ultrafine Particle Characteristics in Seven Industrial Plants. *Annals of Occupational Hygiene*, 53 (5): 475-484. doi: 10.1093/annhyg/mep033.

Elihn, K., Berg, P. & Liden, G. (2011). Correlation between airborne particle concentrations in seven industrial plants and estimated respiratory tract deposition by number, mass and elemental composition. *Journal of Aerosol Science*, 42 (2): 127-141. doi: 10.1016/j.jaerosci.2010.12.003.

Eltawahni, H. A., Olabi, A. G. & Benyounis, K. Y. (2011). Investigating the CO2 laser cutting parameters of MDF wood composite material. *Optics and Laser Technology*, 43 (3): 648-659. doi: 10.1016/j.optlastec.2010.09.006.

Ervik, T. K., Benker, N., Weinbruch, S., Skogstad, A., Thomassen, Y., Ellingsen, D. G. & Berlinger, B. (2018). Phase identification of individual crystalline particles by combining EDX and EBSD: application to workplace aerosols. *Analytical and Bioanalytical Chemistry*, 410 (11): 2711-2721. doi: 10.1007/s00216-018-0949-2.

Ervik, T. K. (2021). *X-ray diffraction analysis of PM from laser cutting* (01.07.2021).

Floros, N. (2018). Welding fume main compounds and structure. *Welding in the World*, 62 (2): 311-316. doi: 10.1007/s40194-018-0552-3.

Genna, S., Menna, E., Rubino, G. & Tagliaferri, V. (2020). Experimental Investigation of Industrial Laser Cutting: The Effect of the Material Selection and the Process Parameters on the Kerf Quality. *Applied Sciences-Basel*, 10 (14). doi: ARTN 4956

10.3390/app10144956.
Gibb, H. J., Lees, P. S. J., Pinsky, P. F. & Rooney, B. C. (2000). Lung cancer among workers in chromium chemical production. *American Journal of Industrial Medicine*, 38 (2): 115-126. doi: Doi 10.1002/1097-0274(200008)38:2<115::Aid-Ajim1>3.3.Co;2-P.
Goldstein, J. I., Newbury, D. E., Michael, J. R., Ritchie, N. W. M., Scott, J. H. J. & Joy, D. C. (2018). *Scanning electron microscopy and x-ray microanalysis*, vol. 4 th. New York, USA: Springer Science.
Graeme, K. A. & Pollack, C. V. (1998). Heavy metal toxicity, Part II: Lead and metal fume fever. *The Journal of Emergency Medicine*, 16 (2): 117-177.
Hamilton, N. E. & Ferry, M. (2018). ggtern: Ternary Diagrams Using ggplot2. *Journal of Statistical Software*, 87: 17.
Hammer, S. E. (2019). *Pilotstudie - Laserskjæring av metall*: The National Institute of Occupational Health (STAMI). Unpublished manuscript.
Helsel, D. R. (2005). More than obvious: Better methods for interpreting nondetect data. *Environmental Science & Technology*, 39 (20): 419a-423a. doi: DOI 10.1021/es053368a.
Helsel, D. R. (2006). Fabricating data: How substituting values for nondetects can ruin results, and what can be done about it. *Chemosphere*, 65 (11): 2434-2439. doi: 10.1016/j.chemosphere.2006.04.051.
Isaxon, C., Pagels, J., Gudmundsson, A., Asbach, C., John, A. C., Kuhlbusch, T. A. J., Karlsson, J. E., Kammer, R., Tinnerberg, H., Nielsen, J., et al. (2009). Characteristics of Welding Fume Aerosol Investigated in Three Swedish Workshops. *Inhaled Particles X*, 151.
Jenkins, N. T. & Eagar, T. W. (2005). Chemical analysis of welding fume particles - Airborne particle size is the most important factor in determining the accuracy of a method for chemical analysis. *Welding Journal*, 84 (6): 87s-93s.
Jolliffe, I. T. (2002). *Principal component analysis*, vol. 2. New York, USA: Springer.
Keyter, M., van Der Merwe, A. & Franken, A. (2019). Particle size and metal composition of gouging and lancing fumes. *Journal of Occupational and Environmental Hygiene*, 16 (9): 643-655. doi: 10.1080/15459624.2019.1639719.
Knutson, E. O. & Whitby, K. T. (1975). Aerosol classification by electric mobility: apparatus, theory, and applications. *Journal of Aerosol Science*, 6 (6): 443-451.
Kulkarni, P., Baron, P. A. & Willeke, K. (2011). *Aerosol Measurement: Principles, Techniques, and Applications*. 3. ed. Hoboken, New Jersey, USA: John Wiley & Sons.
Linge, K. L. & Jarvis, K. E. (2009). Quadrupole ICP-MS: Introduction to Instrumentation, Measurement Techniques and Analytical Capabilities. *Geostandards and Geoanalytical Research*, 33 (4): 445-467. doi: DOI 10.1111/j.1751-908X.2009.00039.x.
Majumdar, J. D. & Manna, I. (2013). Introduction to Laser-Assisted Fabrication of Materials. In vol. 161 *Laser-Assisted Fabrication of Materials*. New York, USA: Springer.
Maricq, M. M., Podsiadlik, D. H. & Chase, R. E. (2000). Size distributions of motor vehicle exhaust PM: A comparison between ELPI and SMPS measurements. *Aerosol Science and Technology*, 33 (3): 239-260. doi: Doi 10.1080/027868200416231.
May, T. W. & Wiedmeyer, R. H. (1998). A table of polyatomic interferences in ICP-MS. *Atomic Spectroscopy*, 19 (5): 150-155.
McCarrick, S., Wei, Z., Moelijker, N., Derr, R., Persson, K. A., Hendriks, G., Wallinder, I. O., Hedberg, Y. & Karlsson, H. L. (2019). High variability in toxicity of welding fume nanoparticles from stainless steel in lung cells and reporter cell lines: the role of particle reactivity and solubility. *Nanotoxicology*, 13 (10): 1293-1309. doi: 10.1080/17435390.2019.1650972.
McNeilly, J. D., Heal, M. R., Beverland, I. J., Howe, A., Gibson, M. D., Hibbs, L. R., MacNee, W. & Donaldson, K. (2004). Soluble transition metals cause the pro-inflammatory effects of welding fumes in vitro. *Toxicology and Applied Pharmacology*, 196 (1): 95-107. doi: 10.1016/j.taap.2003.11.021.
Mehta, R. (2012). Interactions, Imaging and Spectra in SEM. In Kazmiruk, V. (ed.) *Scanning Electron Microscopy*, p. 830: InTech.

Michael, J. R. & Goehner, R. P. (2001). Electron backscatter diffraction: A powerful tool for phase identification in the SEM. *Advances in Materials Problem Solving with the Electron Microscope*, 589: 39-49.

Molchanova, Y. S., Bychkov, N. A. & Chernyayev, S. I. (2015). Producing orifices in structural materials by plasma, waterjet and laser cutting and piercing. *Welding International*, 29 (2): 161-164. doi: 10.1080/09507116.2014.897812.

Montaser, A. (1997). *Inductively coupled plasma mass spectrometry*. Washington DC, USA: Wiley-VCH.

Mora, J., Maestre, S., Hernandis, V. & Todoli, J. L. (2003). Liquid-sample introduction in plasma spectrometry. *Trac-Trends in Analytical Chemistry*, 22 (3): 123-132. doi: 10.1016/S0165-9936(03)00301-7.

Mushtaq, R. T., Wang, Y. N., Rehman, M., Khan, A. M. & Mia, M. (2020). State-Of-The-Art and Trends in CO(2)Laser Cutting of Polymeric Materials-A Review. *Materials*, 13 (17). doi: ARTN 3839 10.3390/ma13173839.

Nayak, R. & Padhye, R. (2016). The use of laser in garment manufacturing: an overview. *Fashion and Textiles*, 3. doi: ARTN 5 10.1186/s40691-016-0057-x.

Norwegian Ministry of Labour and Social affairs. (2013). *Regulations concerning action and limit values for physical and chemical agents in the working environment and classified biological agents (Regulations concerning Action and Limit values)*.

Noskov, A., Ervik, T. K., Tsivilskiy, I., Gilmutdinov, A. & Thomassen, Y. (2020). Characterization of ultrafine particles emitted during laser-based additive manufacturing of metal parts. *Scientific Reports*, 10 (1). doi: ARTN 20989 10.1038/s41598-020-78073-z.

Oprya, M., Kiro, S., Worobiec, A., Horemans, B., Darchuk, L., Novakovic, V., Ennan, A. & Van Grieken, R. (2012). Size distribution and chemical properties of welding fumes of inhalable particles. *Journal of Aerosol Science*, 45: 50-57. doi: 10.1016/j.jaerosci.2011.10.004.

Park, R. M., Bena, J. F., Stayner, L. T., Smith, R. J., Gibb, H. J. & Lees, P. S. J. (2004). Hexavalent chromium and lung cancer in the chromate industry: A quantitative risk assessment. *Risk Analysis*, 24 (5): 1099-1108. doi: DOI 10.1111/j.0272-4332.2004.00512.x.

Pena, A. C., Soler, J. G. & Caicedo, G. R. (1998). The characterization of aerosols generated during the cutting of metallic materials with lasers. *Environmental Technology*, 19 (1): 83-90. doi: Doi 10.1080/09593331908616658.

Pepper, I. L., Gerba, C. P. & Gertry, T. J. (2014). *Environmental Microbiology*. 3 ed. UK: Elsevier Science Publising Co. .

Peters, T. M. & Leith, D. (2003). Concentration measurement and counting e ciency ofthe aerodynamic particle sizer 3321. *Journal of Aerosol Science*, 34: 627-634.

Rayner-Canham, G. & Overton, T. (2014). *Descriptive inorganic chemistry*, vol. 6 th. New York, USA: W.H. Freemann and Company.

Riveiro, A., Mejias, A., Soto, R., Quintero, F., del Val, J., Boutinguiza, M., Lusquinos, F., Pardo, J. & Pou, J. (2016). CO2 laser cutting of natural granite. *Optics and Laser Technology*, 76: 19-28. doi: 10.1016/j.optlastec.2015.07.018.

Shoeb, M., Kodali, V., Farris, B., Bishop, L. M., Meighan, T., Salmen, R., Eye, T., Roberts, J. R., Zeidler-Erdely, P., Erdely, A., et al. (2017). Evaluation of the molecular mechanisms associated with cytotoxicity and inflammation after pulmonary exposure to different metal-rich welding particles. *Nanotoxicology*, 11 (6): 725-736. doi: 10.1080/17435390.2017.1349200.

Skoog, D. A., West, D. M., Holler, J. F. & Crouch, S. R. (2014). *Fundamentals of analytical chemistry*. Belmont, Ca USA: Brooks/Cole, Cengage Learning.

Skoog, D. A., Holler, J. F. & Crouch, S. R. (2018). *Principles of Instrumental Analsysis*. 7 ed. Boston, USA: Brooks/Cole, Cengage Learning.

Small, J. A. & Michael, J. R. (2001). Phase identification of individual crystalline particles by electron backscatter diffraction. *Journal of Microscopy-Oxford*, 201: 59-69. doi: DOI 10.1046/j.1365-2818.2001.00788.x.

Solinov, E. F., Solinov, V. F., Buchanov, V. V., Kustov, M. E., Murav'ev, E. N. & Revenko, V. I. (2015). Application of Laser Technology for Cutting Glass Articles. *Glass and Ceramics*, 71 (9-10): 306-308. doi: 10.1007/s10717-015-9675-9.

Sowards, J. W., Ramirez, A. J., Dickinson, D. W. & Lippold, J. C. (2010). Characterization of Welding Fume from SMAW Electrodes - Part II. *Welding Journal*, 89 (4): 82s-90s.

Stanislawska, M., Halatek, T., Cieslak, M., Kaminska, I., Kuras, R., Janasik, B. & Wasowicz, W. (2017). Coarse, fine and ultrafine particles arising during welding - Analysis of occupational exposure. *Microchemical Journal*, 135: 1-9. doi: 10.1016/j.microc.2017.06.021.

Taube, F. (2013). Manganese in Occupational Arc Welding Fumes-Aspects on Physiochemical Properties, with Focus on Solubility. *Annals of Occupational Hygiene*, 57 (1): 6-25. doi: 10.1093/annhyg/mes053.

Team, R. C. (2018). *R: A Language and Environment for Statistical Computing*: R Foundation for Statistical Computing, Vienna, Austria.

Thomassen, Y., Koch, W., Dunkhorst, W., Ellingsen, D. G., Skaugset, N. P., Jordbekken, L., Drablos, P. A. & Weinbruch, S. (2006). Ultrafine particles at workplaces of a primary aluminium smelter. *Journal of Environmental Monitoring*, 8 (1): 127-133. doi: 10.1039/b514939h.

Tronsmo, A. (2016). *Innføring i mikrobiologi*. Oslo, Norway: Universitetsforlaget.

TSI. (2002). *Model 3010 Condensation Particle Counter - Instruction Manual*. Incorporated, T. (ed.), 103. Shoreview, MN, USA.

TSI. (2004). *Model 3321Aerodynamic Particle Sizer Spectrometer - Instruction Manual* Incorporated, T. (ed.). Shoreview, MN, USA. p. 109.

Ullmann, M., Friedlander, S. K. & Schmidt-Ott, A. (2002). Nanoparticle formation by laser ablation. *Journal of Nanoparticle Research*, 4 (6): 499-509. doi: Doi 10.1023/A:1022840924336.

Vanderwerf, D. F. (2017). *The Story of Light Science - From Early Theories to Today's Extraordinary Applications*. Switzerland: Springer.

Walter, D., Berges, M. G. M., Kreyling, W. G., Korinth, G., Drexler, H., Landsiedel, R., Heinrich, U., Hartwig, A., Schins, R., Pauluh, J., et al. (2013). *Nanomaterials*. In (DFG), D. F. (ed.). Germany.

Wang, J., Hoang, T., Floyd, E. L. & Regens, J. L. (2017). Characterization of Particulate Fume and Oxides Emission from Stainless Steel Plasma Cutting. *Annals of Work Exposures and Health*, 61 (3): 311-320. doi: 10.1093/annweh/wxw031.

Wang, S. C. & Flagan, R. C. (1990). Scanning Electrical Mobility Spectrometer. *Aerosol Science and Technology*, 13 (2): 230-240. doi: Doi 10.1080/02786829008959441.

Wickman, H., Averick, M., Bryan, J., Chang, W., McGowan, L. D., Francois, R., Grolemund, G., Hayes, A., Henry, L., Hester, J., et al. (2019). Welcome to the Tidyverse. *Journal of Open Source Software*, 4 (43): 6.

Wiedensohler, A., Birmili, W., Nowak, A., Sonntag, A., Weinhold, K., Merkel, M., Wehner, B., Tuch, T., Pfeifer, S., Fiebig, M., et al. (2012). Mobility particle size spectrometers: harmonization of technical standards and data structure to facilitate high quality long-term observations of atmospheric particle number size distributions. *Atmospheric Measurement Techniques*, 5 (3): 657-685. doi: 10.5194/amt-5-657-2012.

Wilkinson, A. J. & Britton, T. B. (2012). Strains, planes, and EBSD in materials science. *Materials Today*, 15 (9): 366-376. doi: Doi 10.1016/S1369-7021(12)70163-3.

Yassi, A., Kjellstrom, T., Kok, T. & Guidotti, T. L. (2001). *Basic Environmental health*. New York, USA: Oxford University Press.

Yilbas, B. S., Shaukat, M. M. & Ashraf, F. (2017). Laser cutting of various materials: Kerf width size analysis and life cycle assessment of cutting process. *Optics and Laser Technology*, 93: 67-73. doi: 10.1016/j.optlastec.2017.02.014.

Yoon, C. S., Paik, N. W., Kim, J. H. & Chae, H. B. (2009). Total and Soluble Metal Contents in Flux-Cored Arc Welding Fumes. *Aerosol Science and Technology*, 43 (6): 511-521. doi: 10.1080/02786820902773669.

Zeidler-Erdely, P. C., Erdely, A. & Antonini, J. M. (2012). Immunotoxicology of arc welding fume: Worker and experimental animal studies. *Journal of Immunotoxicology*, 9 (4): 411-425. doi: 10.3109/1547691x.2011.652783.

Supplement 1 Certified reference material ICP-MS

The measured concentrations and calculates mass fractions determined through ICP-MS analysis of CRM materials were found sufficiently good in terms of accuracy (BIAS≤25%) for all elements discussed in Chapter 9. The certified values, measured concentrations and BIAS are presented in Table S1.1 to S1.3.

Table S1.1 ICP-MS results from the two steel certified reference materials SSWF-1 and MSWF-1.

Element	Certified mass fraction (% m/m)	Measured (% m/m)	BIAS (%)
SSWF-1 - Stainless steel welding fume (n=3)			
Cr	8.4 ± 0.4	6.6 ± 0.19	-21
Fe	29.8 ± 0.9	23.5 ± 0.87	-21
Mn	22.9 ± 0.5	20.6 ± 0.82	-10
Ni	3.7 ± 0.2	3.2 ± 0.11	-14
MSWF-1 - Mild steel welding (n=3)			
Fe	42.8 ± 0.7	42 ± 2.3	-1.9
Mn	1.48 ± 0.03	1.5 ± 0.1	1.4
Zn	21.7 ± 0.9	22 ± 1.0	1.4

Table S1.2 ICP-MS results for SRM 1880b – Portland Cement. The measured element concentration has been used to calculate the mass fraction of corresponding oxides.

Element	Certified mass fraction (%)	Measured Mass Fraction (%)	BIAS (%)
Al_2O_3	5.183 ± 0.073	4.3	-17
Fe_2O_3	3.681 ± 0.023	3.5	-5.0
MgO	1.176 ± 0.020	1.9	62
Mn_2O_3	0.1981 ± 0.0020	0.12	-39
SO_3	2.710 ± 0.099	2.6	-4.1
TiO_2	0.236 ± 0.012	0.22	-6.8

Table S1.3 ICP-MS results for SPS-SW2 – elements in surface waters. SPS-SW2 was also certified for Cr, Fe and Zn, but the measured values were below the LOD.

Element	Certified value (µg/L)	Measured (µg/L)	BIAS (%)
Al	250 ± 1	1.5×10^2	-40
Cd	2.50 ± 0.02	2.4	-4.0
Cs	10.0 ± 0.05	10	0
Cu	100 ± 1	98	-2.0
Mg	2000 ± 10	1.8×10^3	-15
Mn	50.0 ± 0.3	60	20
Mo	50.0 ± 0.3	46	-8.0
Ni	50.0 ± 0.3	47	-6.0
Pb	25.0 ± 0.1	26	4.0
S	10000 ± 50	1.1×10^4	10
V	50.0 ± 0.3	40	-20

Supplement 2 Gas modes and mass shifts for ICP-MS

All analytes were measured at different isotope masses at different gas modes, whereas some analytes had a mass shift of either +16 m/z or + 32 m/z. The isotope masses of which the results are based on are marked with grey in Table S2.1. A combination of all isotopes was by the software to calculate Pb concentration based on isotope abundance. Si was not determined due to an unusable calibration curve as the HF acid used for decomposition and reacted with the glass nebulizer.

Table S2.1 Mass shift and gas mode used for ICP-MS analysis for analytes and internal standard. Mass shifts used for the results are marked with grey.

Element	Type	Gas mode	Mass shift (amu)
Ag	Analyte	O_2	107→107
		O_2	109→109
Al	Analyte	No gas	27 →27
		O_2	27→27
Cd	Analyte	O_2	111→111
		O_2	114→114
Cr	Analyte	O_2	52→52
		O_2	52→68
Cs	Analyte	O_2	133→133
Cu	Analyte	O_2	63→63
Fe	Analyte	O_2	56→56
		O_2	56→72
		O_2	57→73
Hg	Analyte	O_2	200→200
		O_2	201→201
		O_2	202→202
Li	Analyte	No gas	7→7
		O_2	7→7
Mg	Analyte	No gas	24 →24
		O_2	24→40
		O_2	25→41
Mn	Analyte	O_2	55→55
		O_2	55→71
Mo	Analyte	O_2	95→127
		O_2	98→130

Ni	Analyte	O_2	60→60
		O_2	60→76
Pb	Analyte	O_2	206→206
		O_2	207→207
		O_2	208→208
S	Analyte	No gas	32 →32
		O_2	32→48
		O_2	34→50
Si	Analyte	No gas	28→28
		No gas	29 →29
		O_2	28→44
Sn	Analyte	He	118→118
		O_2	118→118
		O_2	118→134
		O_2	120→120
		O_2	120→1360
Ti	Analyte	O_2	47→63
V	Analyte	O_2	51→67
W	Analyte	O_2	182→214
		O_2	183→215
Zn	Analyte	He	66→66
		O_2	66→66
Bi	Internal standard	No gas	209 →209
		He	209→209
		O_2	209→209
Se	Internal standard	No gas	74 →74
		He	74→74
		O_2	74→74
			74→90
Rh	Internal standard	No gas	103 →103
		He	103→103
		O_2	103→103

Supplement 3 Raw data from ICP-MS analysis

Table S3.1 Results from ICP-MS determination of selected elements in specific material PM collected from inside laser cutter when cutting specific materials and samples taken from the ventilation system, PMventilation.

	Weight	Ag	Al	Cd	Cr	Cs	Cu	Fe	Hg	Li	Mg	Mn	Mo	Ni	Pb	S	Sn	Ti	V	W	Zn
Sample	mg	µg/g	mg/g	µg/g	mg/g	µg/g	mg/g	g/g	µg/g	µg/g	mg/g	mg/g	mg/g	mg/g	mg/g	mg/g	mg/g	mg/g	µg/g	µg/g	mg/g
Black steel 3.2 mm	0.075	11	8.0	1.9	2.7	5.8	6.2	0.49	<LOD	17	1.5	14	0.33	2.5	0.086	0.24	0.038	0.50	60	12	<LOD
Stainless steel 5 mm	0.119	5.4	8.7	3.2	2.0	3.2	0.88	0.60	1.6	13	2.6	8.6	0.062	1.0	0.045	0.56	0.036	0.59	38	7.7	<LOD
Stainless steel 6 mm	0.146	7.0	16	1.9	1.4	3.0	0.94	0.49	0.84	16	7.0	7.2	0.090	1.2	0.047	1.7	0.040	1.0	51	35	<LOD
Stainless steel 15 mm	0.023	13	15	16	1.8	13	1.4	0.48	6.6	53	7.1	7.7	0.14	1.7	0.11	<LOD	0.067	1.1	65	35	<LOD
Steel 1.5 mm	0.527	3.3	2.1	7.2	0.26	0.63	1.1	0.64	0.24	2.4	0.091	2.9	0.040	0.21	0.0071	0.75	0.049	0.11	3.2	2.3	<LOD
Steel 3 mm	0.018	6.9	22	37	0.39	17	0.51	0.52	2.9	29	0.46	12	0.31	1.6	0.024	1.5	0.036	2.0	49	12	<LOD
Aluminium 10 mm	0.106	22	15 x10[1]	7.0	1.3	2.6	76	0.14	0.67	3.7	11	3.9	0.11	0.65	41	2.4	12	0.79	25	4.1	16
$PM_{ventilation}$ Site 1	0.86	4.9	0.53	<LOD	4.9	0.26	2.6	0.68	0.71	1.9	0.040	15	0.32	4.4	0.027	0.15	0.086	0.059	24	8.0	2.1
$PM_{ventilation}$ Site 2.1	1.21	3.1	17	<LOD	1.6	0.79	2.9	0.59	0.32	1.5	0.95	7.2	0.19	1.3	0.014	0.20	0.082	0.11	14	3.1	24
$PM_{ventilation}$ Site 2.2	0.95	3.3	18	<LOD	1.5	0.34	3.2	0.63	0.47	1.9	1.2	8.0	0.22	1.4	0.016	0.12	0.079	0.077	15	3.2	27
$PM_{ventilation}$ Site 2.3	1.00	2.8	18	<LOD	1.5	0.12	3.1	0.63	0.34	1.7	1.0	7.7	0.21	1.4	0.014	0.13	0.073	0.12	15	3.2	25
LOD		0.000054	0.000011	0.000011	0.0000024	0.0000036	0.00000015	0.000035	0.0000096	0.000014	0.000014	0.0000014	0.00000011	0.0000014	0.00000015	0.000022	0.00000012	0.00000035	0.000028	0.000037	0.00032
LOQ		0.00018	0.000037	0.000036	0.0000080	0.000012	0.00000049	0.00012	0.000032	0.000048	0.000046	0.0000047	0.00000035	0.0000048	0.00000051	0.000072	0.00000038	0.0000012	0.000092	0.00012	0.0011

Table S3.2 Results from ICP-MS determination of selected elements in respirable material matter

	Weight	Ag	Al	Cd	Cr	Cs	Cu	Fe	Hg	Li	Mg	Mn	Mo	Ni	Pb	S	Sn	Ti	V	W	Zn
Sample	mg	mg/g	mg/g	µg/g	mg/g	µg/g	mg/g	g/g	µg/g	µg/g	mg/g	mg/g	mg/g	mg/g	mg/g	mg/g	mg/g	mg/g	µg/g	µg/g	mg/g
Site 1.1	0.054	0.034	40	<LOD	1.3	1.7	0.59	0.072	0.45	39	18	1.5	0.11	1.0	0.16	12	0.062	2.0	91	60	80
Site 1.2	0.051	0.033	42	<LOD	1.5	1.6	0.74	0.12	1.3	39	20	2.2	0.12	1.5	0.14	10	0.0093	2.3	97	56	4.9
Site 2.1	0.031	0.014	66	<LOD	0.12	7.1	0.75	0.15	3.6	26	1.5	1.6	0.087	0.38	0.054	26	0.039	88	34	9.5	<LOD
Site 2.2	0.035	0.19	33	<LOD	<LOD	0.18	0.41	0.038	0.089	13	2.0	0.34	0.011	0.12	0.044	22	<LOD	5.4	33	2.4	35
Site 3.1	0.067	0.060	7.3	0.0041	0.55	0.30	$21x10^{1}$	0.12	1.1	0.60	1.6	2.5	0.053	0.35	$11x10^{1}$	6.1	33	0.058	16	14	5.7
LOD		0.000080	0.000035	0.000056	0.0000058	0.0000034	0.00000055	0.000017	0.0000095	0.000011	0.0000060	0.0000033	0.000000090	0.00000037	0.00000025	0.0000059	0.00000062	0.0000010	0.000016	0.000018	0.00011
LOQ		0.00027	0.00012	0.00019	0.000019	0.000011	0.0000018	0.000055	0.000032	0.000036	0.000020	0.000011	0.00000030	0.0000012	0.00000082	0.000020	0.0000021	0.0000034	0.000053	0.000061	0.000036

Supplement 4 Comparing SMPS data

The number of cycles varied greatly between materials depending on the duration of cutting, as one sampling cycle in the SMPS lasted one minute and 20 seconds. The average particle size concentrations collected during cutting of 0.5 mm aluminium-based plates was for instance based on two cycles, while the largest dataset (6 mm stainless steel) was based on 91 sampling cycles, see Table S4.1 for all processing periods of different material. An evaluation was thereby made to compare two consecutive cycles to an overall mean-

Six tests were conducted whereas one test value consisted of the mean of two random consecutive sampling cycles. The tests were compared with the overall mean of all sampling cycles of that material, see Figure S4.1. Stainless steel (6 mm) was chosen for the evaluation as it has the longest processing time. The test showed that the particle size distribution was similar four of the randomly picked cycles and the mean. Test 4 and 5 however, showed peak concentrations at a lower d_{mob}. One out of six tests (random cycle number 6) had a peak particle concentration higher than the mean, while the other tests had either similar or lower peak particle concentrations.

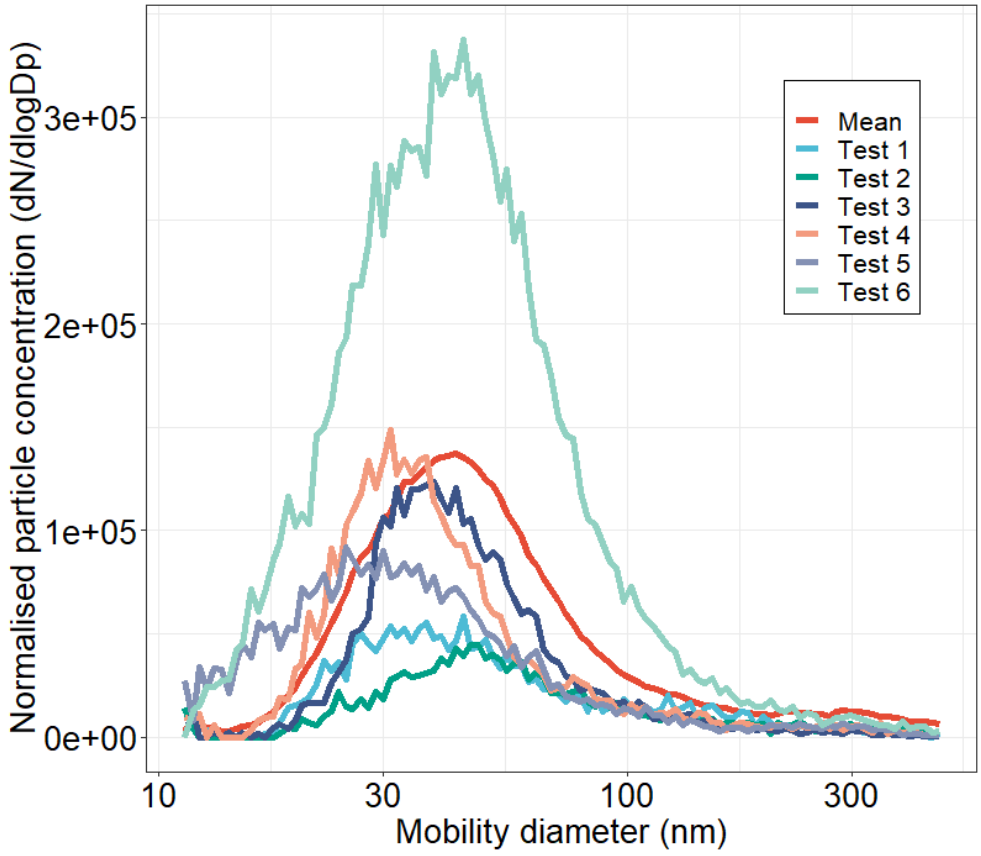

Figure S4.1 Comparing six tests of two consecutive measurements from SMPS with the overall mean of 91 measurements on the same material (Stainless steel 6 mm).

Table S4.1 Plate materials and the time of which the process lasted. The time includes potential changing of plates but are excluded other breaks in the cutting process.

Material	Processing time
Acid-proof steel 3 mm	9 minutes
Aluminium 0.5 mm	4 minutes
Aluminium 10 mm	3 hours and 7 minutes
Aluminium 10 mm and black steel with teflon coating 2.3 mm simultaneously	1 hour and 40 minutes
Black steel 3.2 mm	54 minutes
Stainless steel 15 mm	42 minutes
Stainless steel 5 mm	1 hour and 31 minutes
Stainless steel 6 mm	3 hours and 20 minutes
Steel 1.5mm with carbon-based oil	3 hours
Steel 2 mm cold-treated	12 minutes
Steel 3 mm	1 hour and 18 minutes
Steel 3 mm heat-treated	6 minutes
Titanium plate 4 mm	4 minutes

Supplement 5 Additional secondary electron images

Secondary electron images from cutting a 0.5 mm aluminium based was excluded from the result due to an overload of particles, as seen in Figure S5.1.

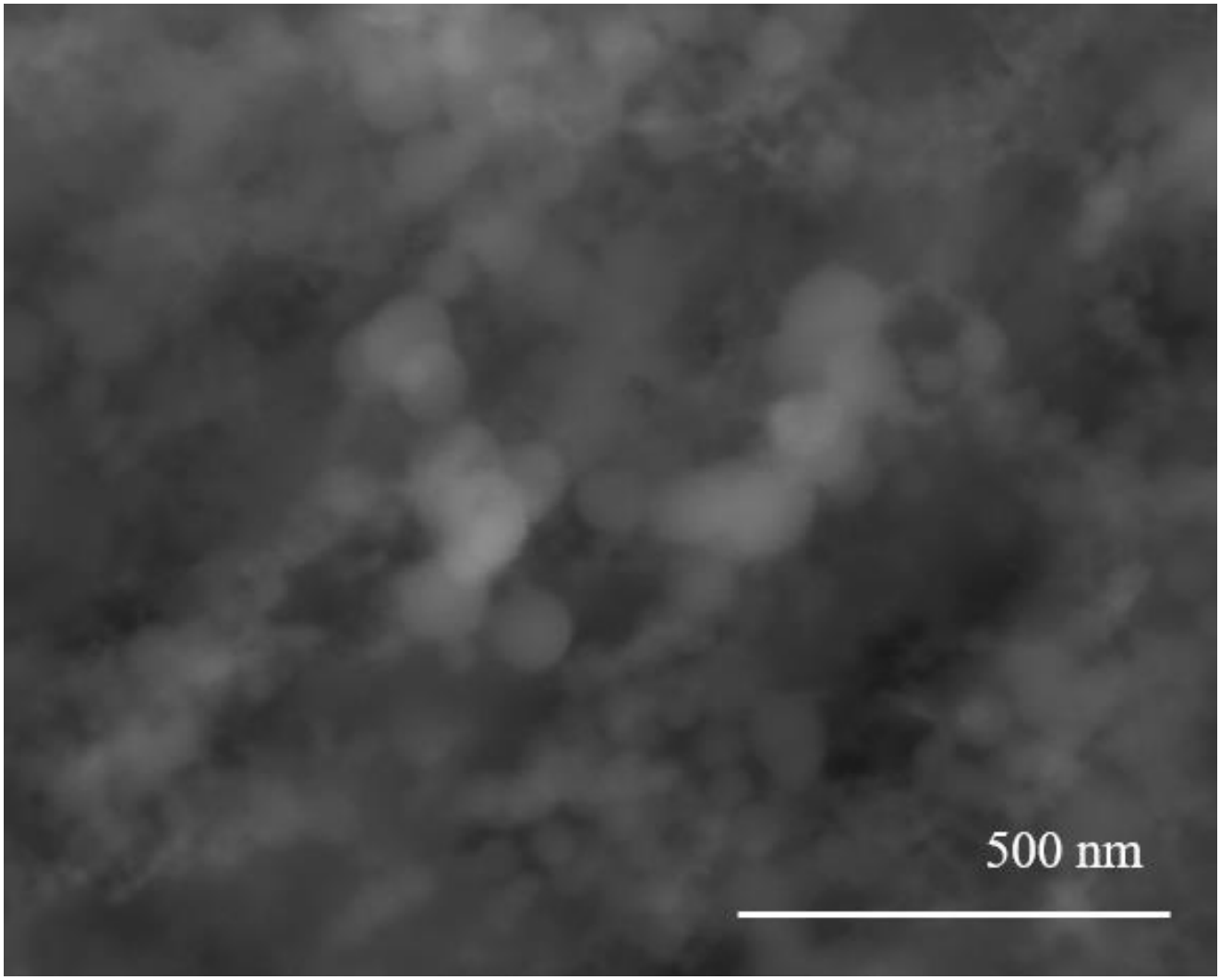

Figure S5.1 Secondary electron image of particles from cutting a 0.5 mm aluminium based plate. Due to stacking on the TEM filer are agglomerates/aggregates not visible, but primary particles of different sizes can be seen.

Norges miljø- og biovitenskapelige universitet
Noregs miljø- og biovitskapelege universitet
Norwegian University of Life Sciences

Postboks 5003
NO-1432 Ås
Norway